Supporting Information

Donor-free 9-aluminafluorenes: molecular structures and reactivity

Paula L. Lückert, Jannik Gilmer, Alexander Virovets, Hans-Wolfram Lerner, and Matthias Wagner*

Institut für Anorganische und Analytische Chemie, Goethe-Universität Frankfurt, Max-von-Laue-Straße 7, D-60438 Frankfurt (Main), Germany

*To whom correspondence should be addressed. Email: matthias.wagner@chemie.uni-frankfurt.de

Table of Contents

1 Experimental details and characterization data

General considerations. All reactions, manipulations, and analyses of air- and moisture-sensitive compounds were carried out under an atmosphere of dry argon or nitrogen using Schlenk techniques or in an argon- or nitrogen-filled glovebox. *n*-Hexane and *n*-pentane was dried over Na metal, C_6H_6, Et_2O, and THF were dried over Na/benzophenone. $C_2H_4Cl_2$ and *ortho*-difluorobenzene (*o*DFB) were distilled from CaH_2. Prior to use, the solvents were degassed by applying three freeze-pump-thaw cycles and stored over molecular sieves (3 Å). Pyridine (py) was stored over molecular sieves (3 Å). C_6D_6 and Tol-d_8 were dried over Na-K alloy without benzophenone (2–3 d), degassed as described above and stored over molecular sieves (3 Å). $CDCl_3$ and CD_2Cl_2 were stored over molecular sieves (3 Å). All other commercially available reagents were used as received. 2,2'-Dibromo-4,4'-di-*tert*-butylbiphenyl,[S1] 2,2'-dilithio-4,4'-di-*tert*-butylbiphenyl[S2] and 2,4,6-tri-*tert*-butylphenyllithium (Mes*Li)[S3] were synthesized according to literature procedures.

If not stated otherwise, NMR spectra were recorded at 298 K using the following spectrometers: Bruker *Avance™ II 300* or Bruker *Avance™ III 500 HD.* Chemical shift values are referenced to (residual) solvent signals ($^1H/^{13}C\{^1H\}$; C_6D_6: δ = 7.16/128.06 ppm; Tol-d_8: δ = 2.08/137.48 ppm; $CDCl_3$: δ = 7.26/77.16 ppm; CD_2Cl_2: δ = 5.32/53.84 ppm), external $SnMe_4$ (0.00 ppm), or external $Al(NO_3)_3$ (0.00 ppm).[S4] Abbreviations: s = singlet, d = doublet, dd = doublet of doublets, t = triplet, m = multiplet, br = broad, n.o. = not observed. Resonances of carbon atoms attached to aluminum atoms were typically broadened and sometimes only observed in ^1H-^{13}C-HMBC NMR experiments due to the quadrupolar relaxation of the ^{27}Al nucleus. Resonance assignments were aided by ^1H-^1H-COSY, ^1H-^{13}C-HSQC,^1H-^{13}C-HMBC, ^1H-^{13}C-H2BC, and ^1H-^{119}Sn-HMBC NMR experiments.

Elemental analyses (%CHN) were performed at the University of Gießen on a Thermo Fisher Scientific *FlashEA* 1112 Elemental Analyzer.

1.1 Synthesis of 1

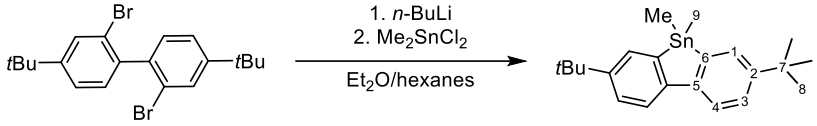

1

Compound **1** was prepared according to the published protocol for *t*Bu-free 9,9-dimethyl-9-stannafluorene with slight modifications.[S5] 2,2'-Dibromo-4,4'-di-*tert*-butylbiphenyl (1.00 g, 2.36 mmol) was placed in a round-bottom flask equipped with a dropping funnel and stirred under vacuum for 10 min. Et_2O (60 mL) was added. *n*-BuLi (2.5 M in hexanes; 2.0 mL, 5.0 mmol) was added dropwise with stirring over 5 min at −78 °C. The mixture was allowed to warm to room temperature and stirred for 3 h. A solution of Me_2SnCl_2 (518 mg, 2.36 mmol) in Et_2O (16 mL) was added dropwise to the stirred reaction mixture at room temperature over a period of 15 min. After stirring overnight at room temperature, a colorless suspension had formed. All volatiles were removed from the reaction mixture under reduced pressure. *n*-Hexane (30 mL) was added to the solid residue and the mixture was sonicated at room temperature for 1 h. The resulting suspension was filtered through Celite® and the solvent was removed from the filtrate under vacuum to obtain **1** as a colorless solid. Yield of **1**: 0.96 g (2.3 mmol, 97 %).

Single crystals of **1** suitable for X-ray diffraction were grown by slow evaporation of a solution of **1** in CH_2Cl_2 and *n*-hexane (Fig. S35).

The reported ^{1}H and ^{13}C NMR shift values are consistent with literature data.[S6]

^{1}H NMR (500.2 MHz, $CDCl_3$): δ = 7.84 (d, $^3J_{H,H}$ = 8.3 Hz, 2H, H-4), 7.67 (d, $^4J_{H,H}$ = 2.2 Hz, 2H, H-1), 7.41 (dd, $^3J_{H,H}$ = 8.3 Hz, $^4J_{H,H}$ = 2.2 Hz, 2H, H-3), 1.37 (s, 18H, H-8), 0.54 (s, 6H, H-9).

^{13}C{^{1}H} NMR (125.8 MHz, $CDCl_3$): δ = 149.8 (C-2), 145.8 (C-5), 140.7 (C-6), 133.0 (C-1), 126.4 (C-3), 121.9 (C-4), 34.8 (C-7), 31.6 (C-8), −8.1 (C-9).

^{119}Sn{^{1}H} NMR (186.5 MHz, $CDCl_3$): δ = −31.4.

1.2 Synthesis of $(2)_2$

Note: $(\mathbf{2})_2$ can be synthesized by one of the two alternative approaches (a) or (b).

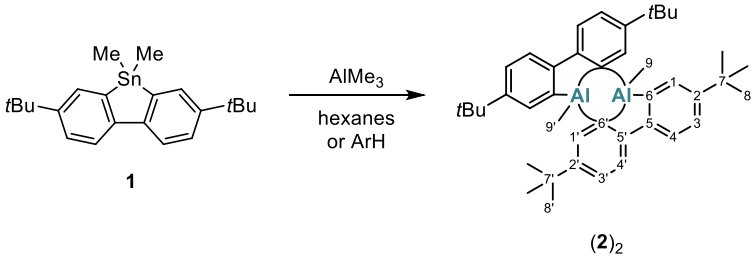

(a) In a nitrogen-filled glovebox, a thick-walled glass ampoule was charged with **1** (1.00 g, 2.42 mmol) and *n*-hexane (3 mL). $AlMe_3$[S7] (2.0 M in hexanes; 1.3 mL, 2.6 mmol) was added at room temperature via syringe. The ampoule was flame-sealed at −196 °C under vacuum and subsequently heated to 140 °C in an oven for 3 d. The ampoule was allowed to cool to room temperature and opened in the glovebox. After 5 min, the obtained suspension was filtered through a frit. The filter cake was washed with *n*-hexane (5 × 1 mL) and dried under vacuum to give a colorless solid. Yield of $(\mathbf{2})_2$: 0.55 g (0.90 mmol, 74 %).

(b) In a nitrogen-filled glovebox, a thick-walled glass ampoule was charged with **1** (0.98 g, 2.4 mmol) and C_6H_6 (3 mL). $AlMe_3$ (2.0 M in toluene; 1.80 mL, 3.60 mmol) was added at room temperature via syringe. The ampoule was flame-sealed at −196 °C under vacuum and subsequently heated to 120 °C in an oven for 3 d. The ampoule was allowed to cool to room temperature and opened in the glovebox. Its content was transferred to a flask. All volatiles were removed under reduced pressure (3 h at 30 °C with stirring), whereupon a solid remained, which was further dried for 2 h at 90 °C in a dynamic vacuum to obtain a pale yellow solid. Yield of $(\mathbf{2})_2$: 0.67 g (1.1 mmol, 91 %).

Single crystals of two polymorphous modifications of *trans*-$(\mathbf{2})_2$ suitable for X-ray diffraction were grown in an argon-filled glovebox by slow evaporation of different solutions of $(\mathbf{2})_2$ from various crystallization attempts: CD_2Cl_2, *n*-hexane (α-*trans*-$(\mathbf{2})_2$; Fig. S36) and toluene (β-*trans*-$(\mathbf{2})_2$; Fig. S37).

<u>*trans*-$(\mathbf{2})_2$ in Tol-d_8:</u>

^{1}H NMR (500.2 MHz, Tol-d_8, –30 °C): δ = 8.62 (d, $^4J_{H,H}$ = 2.2 Hz, 2H, H-1'), 8.19 (d, $^4J_{H,H}$ = 2.1 Hz, 2H, H-1), 7.92 (d, $^3J_{H,H}$ = 8.2 Hz, 2H, H-4), 7.70 (d, $^3J_{H,H}$ = 8.2 Hz, 2H, H-4'), 7.53 (dd, $^3J_{H,H}$ = 8.2 Hz, $^4J_{H,H}$ = 2.1 Hz, 2H, H-3), 7.42 (dd, $^3J_{H,H}$ = 8.2, $^4J_{H,H}$ = 2.2 Hz, 2H, H-3'), 1.47 (s, 18H, H-8 or H-8'), 1.28 (s, 18H, H-8 or H-8'), −0.67 (s, 6H, H-9 and H-9').

^{13}C{^{1}H} NMR (125.8 MHz, Tol-d_8, –30 °C): δ = 162.6 (C-5'), 152.4 (C-6), 149.3 (C-2 and C-2'), 148.4 (C-5), 146.4 (C-1'), 134.2 (C-1), 134.1 (C-3'), 127.6 (C-6'), 127.5 (C-3), 126.1 (C-4'), 122.7 (C-4), 35.0 (C-7 or C-7'), 35.0 (C-7 or C-7'), 31.8 (C-8 or C-8'), 31.5 (C-8 or C-8'), −10.9 (C-9 and C-9').

^{27}Al NMR (130.3 MHz, Tol-d_8, –30 °C): δ = n.o.

trans-(**2**)$_2$ in CD_2Cl_2:

^{1}H NMR (500.2 MHz, CD_2Cl_2, –30 °C): δ = 8.22 (d, $^4J_{H,H}$ = 2.2 Hz, 2H, H-1'), 7.89–7.88 (m, 4H, H-1 and H-4), 7.84 (d, $^3J_{H,H}$ = 8.2 Hz, 2H, H-4'), 7.77 (dd, $^3J_{H,H}$ = 8.2 Hz, $^4J_{H,H}$ = 2.2 Hz, 2H, H-3'), 7.53 (dd, $^3J_{H,H}$ = 8.1 Hz, $^4J_{H,H}$ = 2.2 Hz, 2H, H-3), 1.40 (s, 18H, H-8), 1.36 (s, 18H, H-8'), –1.13 (s, 6H, H-9 and H-9').

^{13}C{^{1}H} NMR (125.8 MHz, CD_2Cl_2, –30 °C): δ = 161.5 (C-5'), 151.6 (br; C-6), 149.3 (C-2'), 149.2 (C-2), 147.7 (C-5), 145.8 (C-1'), 133.8 (C-1 or C-3'), 133.7 (C-1 or C-3'), 127.0 (C-3), 126.8 (C-6'), 125.4 (C-4'), 121.9 (C-4), 34.8 (C-7'), 34.7 (C-7), 31.3 (C-8 and C-8'), –11.6 (br; C-9 and C-9').

^{27}Al NMR (130.3 MHz, CD_2Cl_2, –30 °C): δ = n.o.

cis-(**2**)$_2$ in CD_2Cl_2:

^{1}H NMR (500.2 MHz, CD_2Cl_2, –30 °C): δ = 8.51 (d, $^4J_{H,H}$ = 2.0 Hz, 2H, H-1'), 7.77* (H-3'), 7.39 (d, $^3J_{H,H}$ = 8.2 Hz, 2H, H-4), 6.97 (dd, $^3J_{H,H}$ = 8.2 Hz, $^4J_{H,H}$ = 2.2 Hz, 2H, H-3), 6.82 (d, $^4J_{H,H}$ = 2.2 Hz, 2H, H-1), 1.44 (s, 18H, H-8), 1.11 (s, 18H, H-8'), –0.57 (s, 6H, H-9 and H-9'), n.o.** (H-4'). *) This signal was only detected in the ^{1}H-^{1}H-COSY NMR experiment, because it overlaps with a signal of *trans*-(**2**)$_2$. **) This signal could not be unequivocally identified due to strongly overlapping signals.

^{13}C{^{1}H} NMR (125.8 MHz, CD_2Cl_2, –30 °C): δ = 162.1 (C-5'), 148.7 (br; C-6), 148.0 (C-2), 147.7* (C-2'), 147.6 (C-1'), 147.5 (C-5), 133.3 (C-3'), 132.6 (C-1), 125.8 (C-6'), 125.1 (C-3), 122.0 (C-4), 34.7 (C-7'), 34.1 (C-7), 31.1 (C-8 and C-8'), –8.0 (br; C-9 and C-9'), n.o.** (C-4'). *) This signal was only detected in the ^{1}H-^{13}C-HMBC NMR experiment, because it overlaps with a signal of *trans*-(**2**)$_2$. **) This signal could not be unequivocally identified due to strongly overlapping signals.

^{27}Al NMR (130.3 MHz, CD_2Cl_2, –30 °C): δ = n.o.

Note: H and C atoms belonging to the same *t*Bu-C_6H_3 ring were identified by using 2D NMR experiments. The assignment to a terminal (H/C) vs. Al···Al-bridging ring (H'/C') is based on computed ^{13}C NMR shift values, which show an excellent match (Chapter 4.2).

EA (%): Calculated for the monomer $C_{21}H_{27}Al$ [306.19]: C 82.31, H 8.88; found: C 81.04, H 8.70.

1.3 Determination of the coalescence temperature (T_c) of the *cis*/*trans*-(**2**)$_2$ inversion

Note: The coalescence temperature was determined by analyzing the ^{1}H NMR spectra in (a) CD_2Cl_2 and (b) Tol-d_8.

(a) An NMR tube was charged with (**2**)$_2$ (31 mg) and CD_2Cl_2 (0.5 mL). The NMR tube was flame-sealed under vacuum. ^{1}H NMR spectra were measured at 5 °C, 11 °C, 13 °C, 15 °C, 25 °C, and 32 °C. Comparison of the line shapes of the *tert*-butyl group resonances of *trans*-(**2**)$_2$ revealed a coalescence temperature of approximately 13 °C (Fig. S13).

(b) An NMR tube was charged with (**2**)$_2$ (31 mg) and Tol-d_8 (0.5 mL). The NMR tube was flame-sealed under vacuum. ^{1}H NMR spectra were measured at –15 °C, –5 °C, 5 °C, 15 °C, 20 °C, 25 °C, 35 °C, 45 °C, 55 °C, and 65 °C. Comparison of the line shapes of the *tert*-butyl group resonances of *trans*-(**2**)$_2$ revealed a coalescence temperature of approximately 30 °C (Fig. S14).

1.4 Influence of the solvent on the *cis*/*trans*-(**2**)$_2$ ratio

An NMR tube was charged with (**2**)$_2$ (≈30 mg) and the respective solvent (0.5 mL). The NMR tube was flame-sealed under vacuum.

The more polar the solvent is, the more *cis*-(**2**)$_2$ and the less *trans*-(**2**)$_2$ is present, as is evident from the integral ratios of the Me-groups of the two isomers (Table S1, Fig. S1, S8, S11, S15–S17). This is consistent with the polarity of the compounds, as *cis*-(**2**)$_2$ is slightly polar, while *trans*-(**2**)$_2$ is completely non-polar (Fig. S2).

Table S1: Solvents, polarity indices and integral ratios of the Me-group signals of *trans*-(**2**)$_2$ and *cis*-(**2**)$_2$ based on ^{1}H NMR spectra recorded at −30 °C. *) Since the polarity index of *o*DFB is not known, the index of chlorobenzene is given instead, as it is presumably similar.

Solvent	Polarity index[S8]	*trans*-(**2**)$_2$	*cis*-(**2**)$_2$
Tol-d_8	2.3	0.90	0.10
*o*DFB	2.7*	0.85	0.15
CD_2Cl_2	3.4	0.82	0.18
$C_2H_4Cl_2$	3.7	0.81	0.19
$CDCl_3$	4.4	0.75	0.25

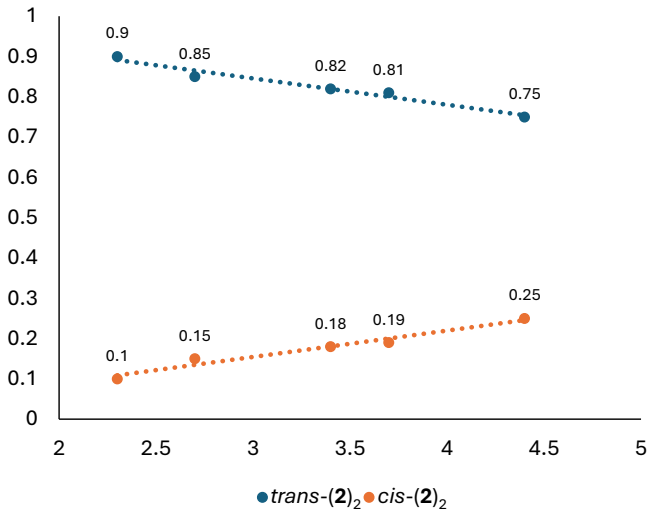

Fig. S1: Plot of the polarity index of a given solvent (Table S1; x axis) against the integral ratio of the Me-groups of *trans*-(**2**)$_2$ and *cis*-(**2**)$_2$, based on ^{1}H NMR spectra recorded at −30 °C (Table S1; y axis).

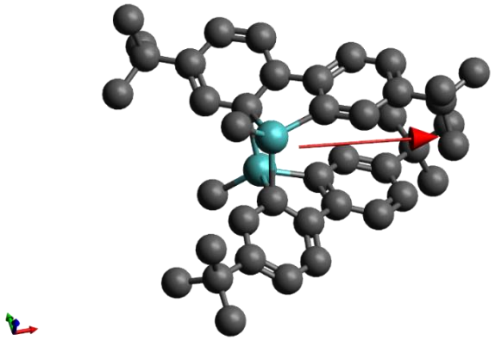

Fig. S2: Dipole moment (red arrow) of the computed molecular structure of *cis*-(**2**)$_2$ (*Avogadro 1.2.0*).[S9]

1.5 Synthesis of 2·do

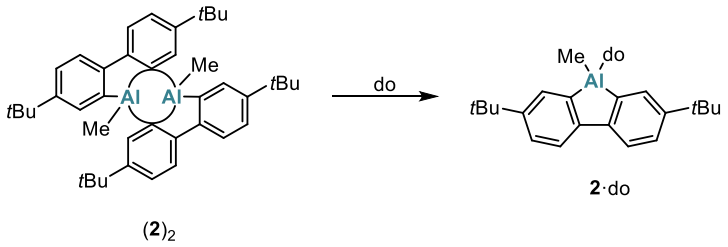

$(\mathbf{2})_2$ **2**·do

General procedure: In an argon-filled glovebox, a round-bottom flask was charged at room temperature with $(\mathbf{2})_2$, the respective solvent, and the donor molecule (Do). The reaction mixture was stirred for 5 min at room temperature inside the glovebox.

1.5.1 Synthesis of 2·OEt_2

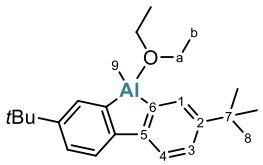

2·OEt_2

$(\mathbf{2})_2$ (18 mg, 30 µmol), C_6H_6 (0.5 mL), Et_2O (0.1 mL, 1 mmol). A dynamic vacuum was applied to obtain **2**·OEt_2 as a colorless solid. Yield of **2**·OEt_2: 22 mg (58 µmol, quantitative).

Single crystals of **2**·OEt_2 suitable for X-ray diffraction were grown in an argon-filled glovebox by slow evaporation of a solution of **2**·OEt_2 in C_6H_6 and *n*-hexane (Fig. S40).

<u>**2**·OEt_2 in C_6D_6 at room temperature:</u>

^{1}H NMR (500.2 MHz, C_6D_6): δ = 8.05 (d, $^3J_{H,H}$ = 8.1 Hz, 2H, H-4), 7.95 (d, $^4J_{H,H}$ = 2.3 Hz, 2H, H-1), 7.46 (dd, $^3J_{H,H}$ = 8.1 Hz, $^4J_{H,H}$ = 2.3 Hz, 2H, H-3), 3.24 (q, $^3J_{H,H}$ = 7.0 Hz, 4H, H-a), 1.44 (s, 18H, H-8), 0.64–0.62 (m, 6H, H-b), −0.20 (s, 3H, H-9).

^{13}C{^{1}H} NMR (125.8 MHz, C_6D_6): δ = 150.3 (C-5), 148.1 (C-2), 147.4 (br, C-6), 133.1 (C-1), 126.0 (C-3), 120.6 (C-4), 67.7 (C-a), 34.6 (C-7), 31.9 (C-8), 13.5 (C-b), −12.0 (br, C-9).

^{27}Al NMR (130.3 MHz, C_6D_6): δ = n.o.

<u>**2**·OEt_2 in CD_2Cl_2 at −30 °C:</u>

^{1}H NMR (500.2 MHz, CD_2Cl_2, −30 °C): δ = 7.69 (d, $^3J_{H,H}$ = 8.2 Hz, 2H, H-4), 7.66 (d, $^4J_{H,H}$ = 2.3 Hz, 2H, H-1), 7.26 (dd, $^3J_{H,H}$ = 8.2 Hz, $^4J_{H,H}$ = 2.3 Hz, 2H, H-3), 3.95 (q, $^3J_{H,H}$ = 7.1 Hz, 4H, H-10), 1.32 (s, 18H, H-8), 1.26 (t, $^3J_{H,H}$ = 7.1 Hz, 6H, H-11), −0. 50 (s, 3H, H-9).

^{13}C{^{1}H} NMR (125.8 MHz, CD_2Cl_2, −30 °C): δ = 149.0 (C-5), 147.9 (C-2), 147.0 (br; C-6), 132.9 (C-1), 125.1 (C-3), 119.5 (C-4), 68.1 (C-10), 34.3 (C-7), 31.2 (C-8), 13.7 (C-11), −12.5 (br; C-9).

^{27}Al NMR (130.3 MHz, C_6D_6, −30 °C): δ = n.o.

EA (%): Calculated for $C_{25}H_{37}AlO$ [380.27]: C 78.91, H 9.80; found: C 77.57, H 9.41.

1.5.2 Synthesis of 2·thf

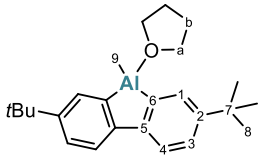

2·thf

(**2**)$_2$ (21 mg, 34 µmol), C_6D_6 (0.5 mL), THF (5.6 µL, 69 µmol). NMR spectroscopy showed a quantitative conversion of (**2**)$_2$ to **2**·thf.

^{1}H NMR (500.2 MHz, C_6D_6): δ = 8.06 (d, $^3J_{H,H}$ = 8.2 Hz, 2H, H-4), 7.98 (d, $^4J_{H,H}$ = 2.3 Hz, 2H, H-1), 7.48 (dd, $^3J_{H,H}$ = 8.2 Hz, $^4J_{H,H}$ = 2.3 Hz, 2H, H-3), 3.33–3.30 (m, 4H, H-a), 1.45 (s, 18H, H-8), 0.78–0.76 (m, 4H, H-b), –0.15 (s, 3H, H-9).

^{13}C{^{1}H} NMR (125.8 MHz, C_6D_6): δ = 150.4 (C-5), 148.2 (C-2), 147.3 (br; C-6), 133.0 (C-1), 126.0 (C-3), 120.6 (C-4), 71.3 (C-a), 34.7 (C-7), 32.0 (C-8), 24.7 (C-b), –12.6 (br; C-9).

^{27}Al NMR (130.3 MHz, C_6D_6): δ = n.o.

1.5.3 Synthesis of 2·py

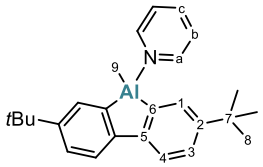

2·py

(**2**)$_2$ (17 mg, 28 µmol), C_6H_6 (0.5 mL), py (6.5 µL, 80 µmol). A dynamic vacuum was applied to obtain **2**·py as a colorless solid. Yield of **2**·py: 22 mg (52 µm, 93 %). *Note*: Considering the co-crystallized C_6H_6 in the crystal lattice, the molar mass of **2**·py × $(C_6H_6)_{0.5}$ was used to calculate the yield.

Single crystals of **2**·py × $(C_6H_6)_{0.5}$ suitable for X-ray diffraction were grown in an argon-filled glovebox through gas-phase diffusion of *n*-hexane into a C_6H_6 solution of **2**·py (Fig. S41).

^{1}H NMR (500.2 MHz, C_6D_6): δ = 8.17 (d, $^3J_{H,H}$ = 8.2 Hz, 2H, H-4), 8.10–8.09 (m, 2H, H-a), 8.04 (d, $^4J_{H,H}$ = 2.3 Hz, 2H, H-1), 7.51 (dd, $^3J_{H,H}$ = 8.2 Hz, $^4J_{H,H}$ = 2.3 Hz, 2H, H-3), 6.46–6.43 (m, 1H, H-c), 6.04–6.01 (m, 2H, H-b), 1.41 (s, 18H, H-8), 0.08 (s, 3H, H-9).

^{13}C{^{1}H} NMR (125.8 MHz, C_6D_6): δ = 150.7 (C-5), 149.4 (br; C-6), 148.2 (C-2), 147.3 (C-a), 139.9 (C-c), 133.2 (C-1), 126.1 (C-3), 125.0 (C-b), 120.8 (C-4), 34.7 (C-7), 31.9 (C-8), –12.4 (br; C-9).

^{27}Al NMR (130.3 MHz, C_6D_6): δ = n.o.

EA (%): Calculated for $C_{26}H_{32}AlN$ [385.24]: C 81.00, H 8.37, N 3.63; found: C 79.70, H 8.20, N 3.88.

1.6 Synthesis of $(3)_2$

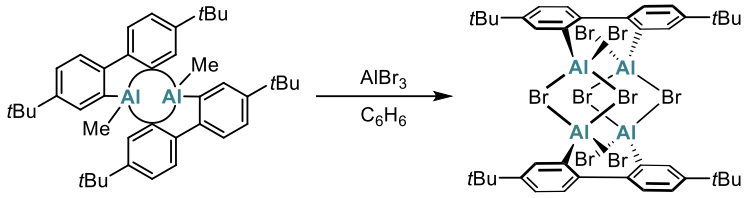

$(\mathbf{2})_2$ $(\mathbf{3})_2$

$AlBr_3$[S7] (0.90 g, 3.4 mmol) was added to a stirred solution of $(\mathbf{2})_2$ (0.50 g, 0.81 mmol) in C_6H_6 (4 mL) at room temperature inside a nitrogen-filled glovebox. After stirring overnight, volatiles were removed under reduced pressure at room temperature (10^{-3} Torr). The by-product $MeAlBr_2$[S7] and the unconsumed $AlBr_3$ were afterwards completely sublimed off from the remaining crude product at higher temperatures (130 °C, 2.5 h, 10^{-3} Torr; Fig. S26). The oily residue was dissolved in C_6H_6 (4 mL) and freeze-dried to furnish $(\mathbf{3})_2$ as a yellow solid. Yield of $(\mathbf{3})_2$: 0.98 g (0.77 mmol, 95 %).

Single crystals of $(\mathbf{3})_2$ suitable for X-ray diffraction were grown in an argon-filled glovebox by slow evaporation of a solution of $(\mathbf{3})_2$ in C_6H_6 and *n*-hexane (Fig. S42).

Note: Since the NMR signals of $(\mathbf{3})_2$ were severely broadened in the temperature range between +70 and −30 °C, NMR spectroscopic analysis was not possible (Fig. S27, S28).

EA (%): Calculated for the monomer $C_{20}H_{24}Al_2Br_4$ [633.82]: C 37.65, H 3.79; found: C 37.24, H 3.78.

1.7 Reaction of $(3)_2$ with Et_2O to furnish $4{\cdot}OEt_2$

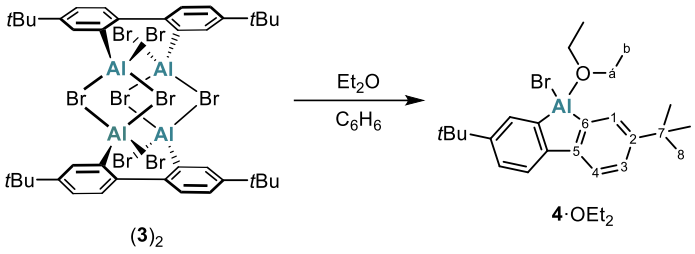

$(\mathbf{3})_2$ $\mathbf{4}{\cdot}OEt_2$

An NMR tube was charged with $(\mathbf{3})_2$ (20 mg, 16 µmol), C_6H_6 (0.5 mL), and Et_2O (0.1 mL, 0.9 mmol) at room temperature inside an argon-filled glovebox, whereupon $\mathbf{4}{\cdot}OEt_2$ precipitated as a colorless solid in essentially quantitative yield.

^{1}H NMR (500.2 MHz, $CDCl_3$): δ = 7.74 (d, $^3J_{H,H}$ = 8.2 Hz, 2H, H-4), 7.64 (d, $^4J_{H,H}$ = 2.2 Hz, 2H, H-1), 7.34 (dd, $^3J_{H,H}$ = 8.2 Hz, $^4J_{H,H}$ = 2.2 Hz, 2H, H-3), 4.26 (br; 4H, H-a), 1.41 (t, $^3J_{H,H}$ = 7.2 Hz, 6H, H-b), 1.34 (s, 18H, H-8).

^{13}C{^{1}H} NMR (125.8 MHz, $CDCl_3$): δ = 149.0 (C-2), 148.3 (C-5), 141.4* (C-6), 132.5 (C-1), 126.5 (C-3), 120.4 (C-4), 70.0 (br; C-a), 34.6 (C-7), 31.6 (C-8), 14.1 (C-b). *) This signal was only detected in the ^{1}H-^{13}C-HMBC NMR experiment.

^{27}Al NMR (130.3 MHz, $CDCl_3$): δ = n.o.

1.8 Reaction of $(3)_2$ with py to furnish 4·py

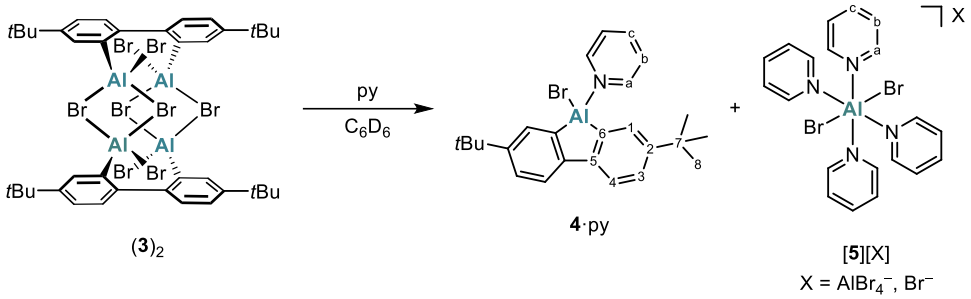

$(\mathbf{3})_2$ **4**·py [**5**][X]
X = $AlBr_4^-$, Br^-

An NMR tube was charged with $(\mathbf{3})_2$ (30 mg, 24 µmol), C_6D_6 (0.5 mL), and py (19 µL, 0.24 mmol) at room temperature inside an argon-filled glovebox. After the NMR tube had been stored at room temperature for 1 d, a colorless solid had precipitated. NMR spectroscopy showed the formation of **4**·py, along with at least one other py-containing species (most likely [**5**][$AlBr_4$] and/or [**5**][Br], which crystallized from the reaction mixture; see Fig. S31, S32).

Single crystals of **4**·py, [**5**][$AlBr_4$], and [**5**][Br] suitable for X-ray diffraction were grown in an argon-filled glovebox by slow evaporation of different solutions from various crystallization attempts: Et_2O and *n*-hexane (**4**·py; Fig. S43), C_6D_6 and *n*-hexane ([**5**][$AlBr_4$]; Fig. S44), and C_6H_6 and *n*-hexane ([**5**][Br]; Fig. S45).

4·py:

^{1}H NMR (500.2 MHz, C_6D_6): δ = 8.48–8.47 (m, H-a)*, 8.05 (d, $^3J_{H,H}$ = 8.2 Hz, 2H, H-4), 8.01 (d, $^4J_{H,H}$ = 2.2 Hz, 2H, H-1), 7.48 (dd, $^3J_{H,H}$ = 8.2 Hz, $^4J_{H,H}$ = 2.2 Hz, 2H, H-3), 6.81–6.78 (m, H-c)*, 6.45–6.43 (m, H-b)*, 1.33 (s, 18H, H-8). *) *Note*: The integral values of the resonances of the aromatic protons of the py ligand are higher than to be expected, likely due to overlap with the py signals of [**5**][X].

^{13}C{^{1}H} NMR (125.8 MHz, C_6D_6): δ = 149.7 (C-5), 149.1 (C-2 or C-a), 149.1 (C-2 or C-a), 143.9 (br; C-6), 137.8 (C-c), 133.0 (C-1), 127.1 (C-3), 124.3 (C-b), 121.1 (C-4), 34.7 (C-7), 31.8 (C-8).

^{27}Al NMR (130.3 MHz, $CDCl_3$): δ = n.o.

[**5**][X]:

^{1}H NMR (500.2 MHz, C_6D_6): δ = 8.48–8.47 (m, H-a), 6.81–6.78 (m, H-c), 6.45–6.43 (m, H-b).

^{13}C{^{1}H} NMR (125.8 MHz, C_6D_6): δ = 149.0 (C-a), 137.7 (C-c), 124.3 (C-b).

^{27}Al NMR (130.3 MHz, $CDCl_3$): δ = n.o.

1.9 Synthesis of 6

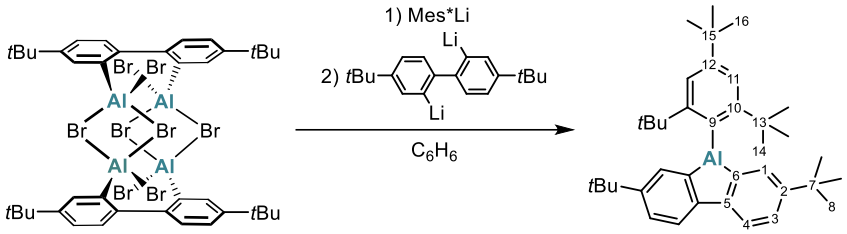

$(\mathbf{3})_2$ **6**

Inside an argon-filled glovebox, Mes*Li (47 mg, 0.19 mmol) was added to a stirred solution of $(\mathbf{3})_2$ (55 mg, 43 µmol) in C_6H_6 (2 mL), whereupon a colorless solid precipitated. After stirring the reaction mixture for 2 min at room temperature, 2,2'-dilithio-4,4'-di-*tert*-butylbiphenyl (28 mg, 0.10 mmol) was added, whereupon the amount of precipitate increased further. After the reaction mixture had been stirred overnight at room temperature, it was filtered through a 0.45 µm PTFE syringe filter. The remaining solution was freeze-dried to afford a colorless solid. Yield of **6**: 90 mg (0.17 mmol, 97 %).

Single crystals of **6** × C_6H_6 suitable for X-ray diffraction were grown in an argon-filled glovebox by slow evaporation of a solution of **6** in C_6H_6 and *n*-pentane (Fig. S46).

^{1}H NMR (500.2 MHz, C_6D_6): δ = 8.07 (d, $^3J_{H,H}$ = 8.2 Hz, 2H, H-4), 7.92 (d, $^4J_{H,H}$ = 2.2 Hz, 2H, H-1), 7.55 (s, 2H, H-11), 7.49 (dd, $^3J_{H,H}$ = 8.2, $^4J_{H,H}$ = 2.2 Hz, 2H, H-3), 1.47 (s, 18H, H-14), 1.34 (s, 9H, H-16), 1.32 (s, 18H, H-8).

^{13}C{^{1}H} NMR (125.8 MHz, C_6D_6): δ = 160.6 (C-10), 151.7 (C-12), 149.7 (C-2), 148.9 (C-5), 144.7 (C-6), 132.8 (C-1), 129.1 (br; C-9), 127.3 (C-3), 121.2 (C-4), 120.8 (C-11), 38.2 (C-13), 35.1 (C-15), 34.7 (C-7), 32.6 (C-14), 31.7 (C-8), 31.5 (C-16).

^{27}Al NMR (130.3 MHz, C_6D_6): δ = n.o.

2 Plots of NMR spectra

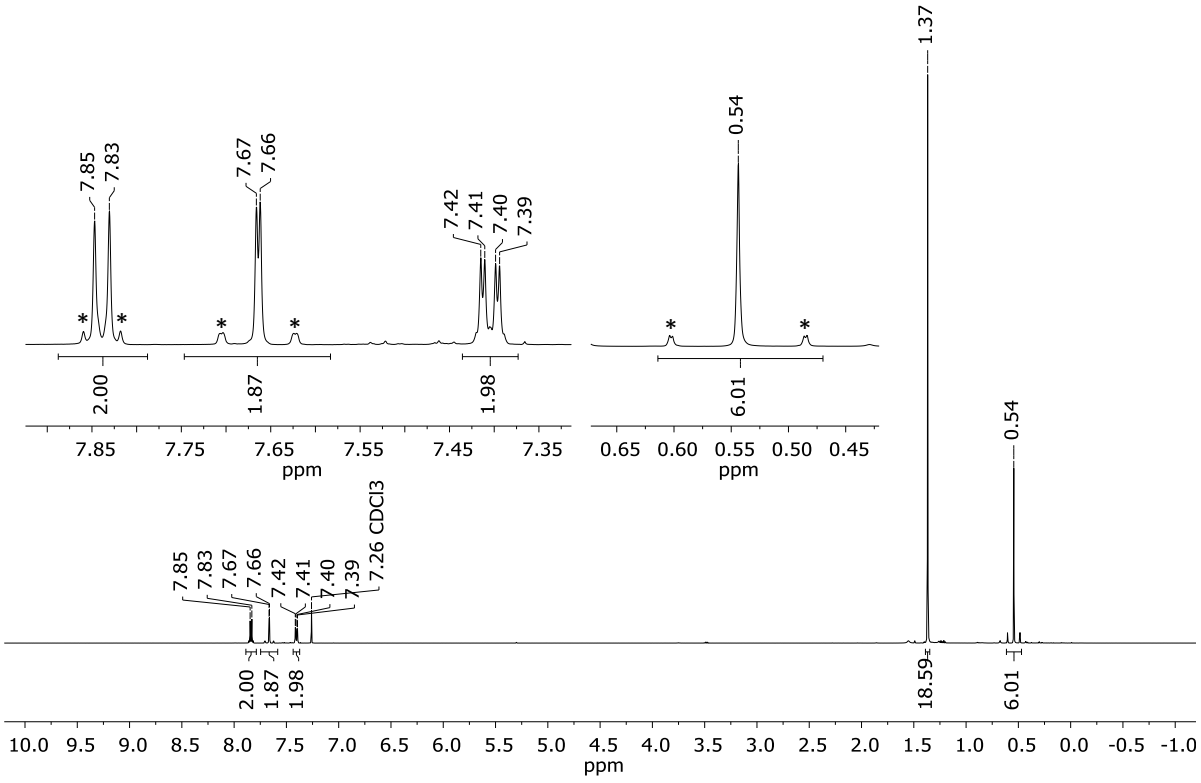

Fig. S3: ^{1}H NMR spectrum of **1** (500.2 MHz, $CDCl_3$). Resonances marked with (*) are $^{117/119}$ Sn satellites.

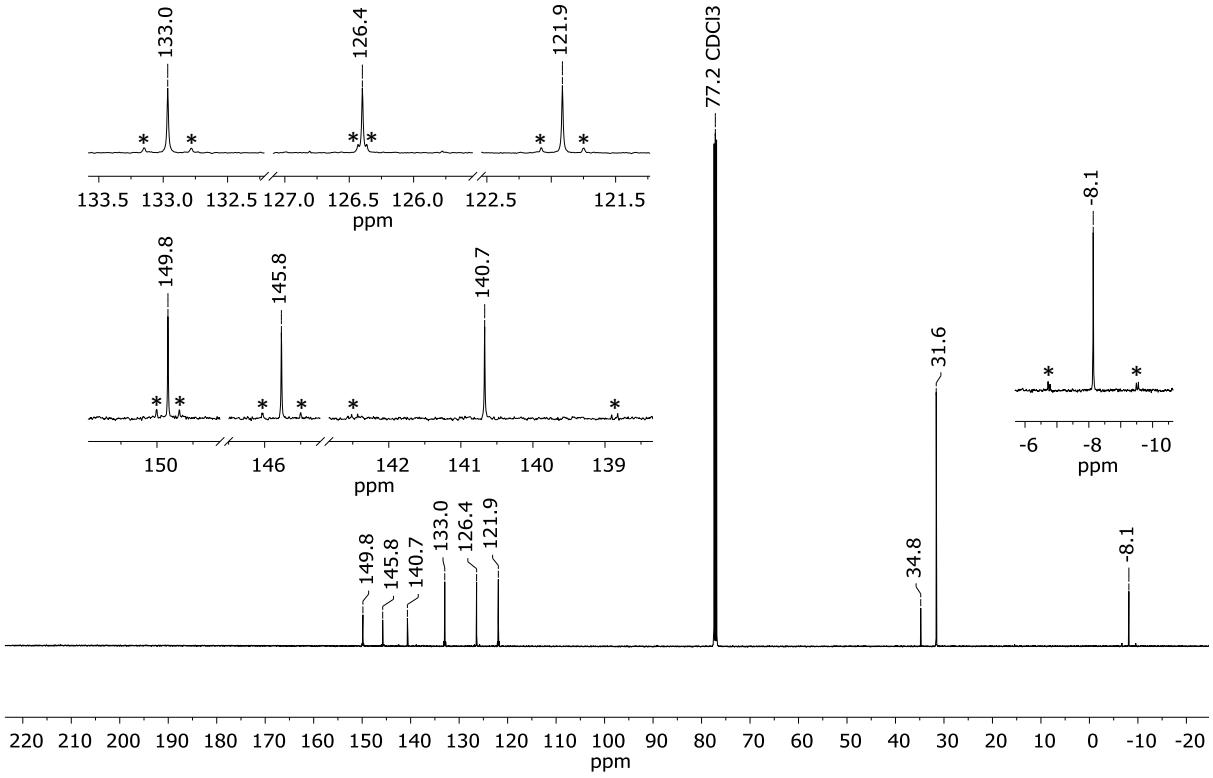

Fig. S4: $^{13}C\{^{1}H\}$ NMR spectrum of **1** (125.8 MHz, $CDCl_3$). Resonances marked with (*) are $^{117/119}$ Sn satellites.

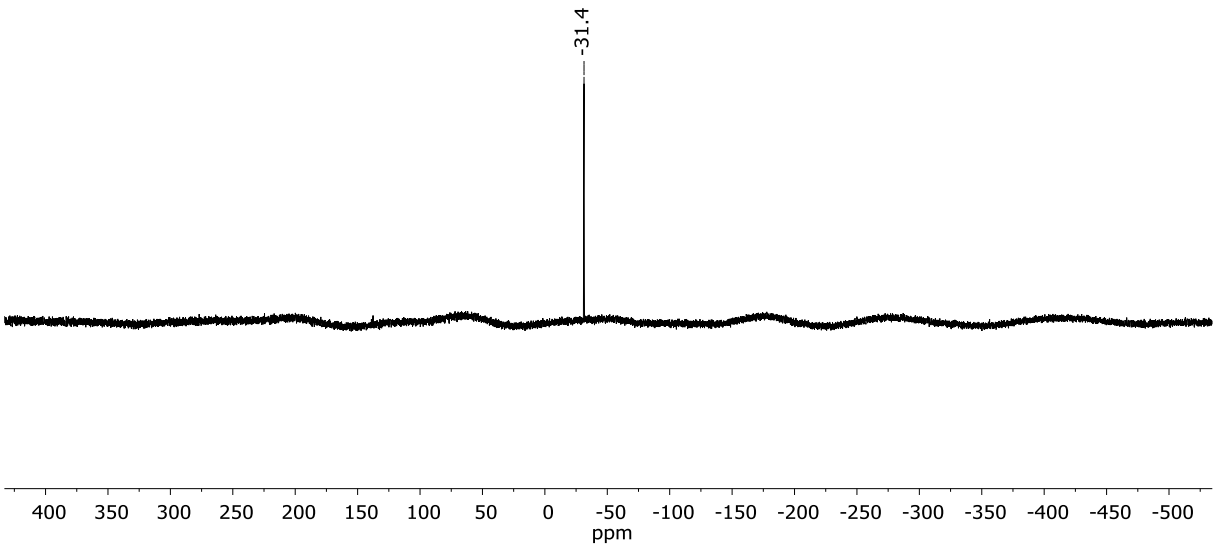

Fig. S5: $^{119}Sn\{^{1}H\}$ NMR spectrum of **1** (186.5 MHz, $CDCl_3$).

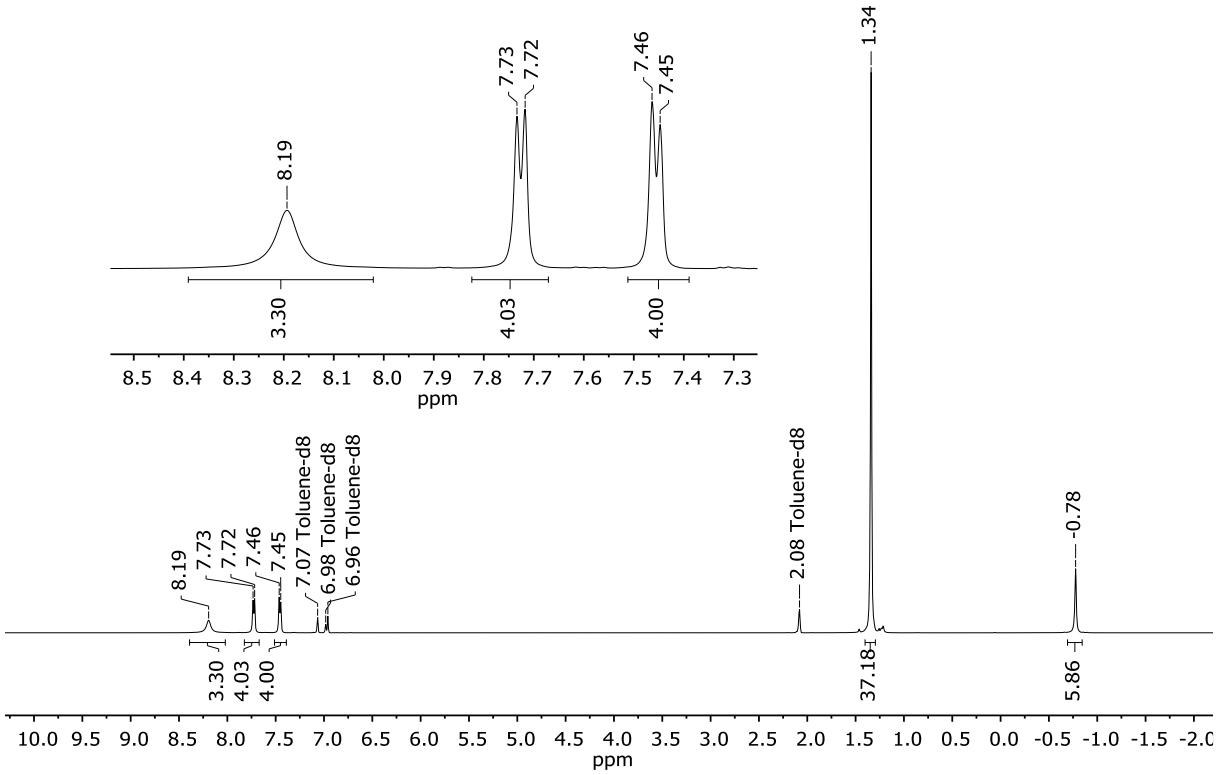

Fig. S6: ^{1}H NMR spectrum of $(\mathbf{2})_2$ (500.2 MHz, Tol-d_8, 70 °C).

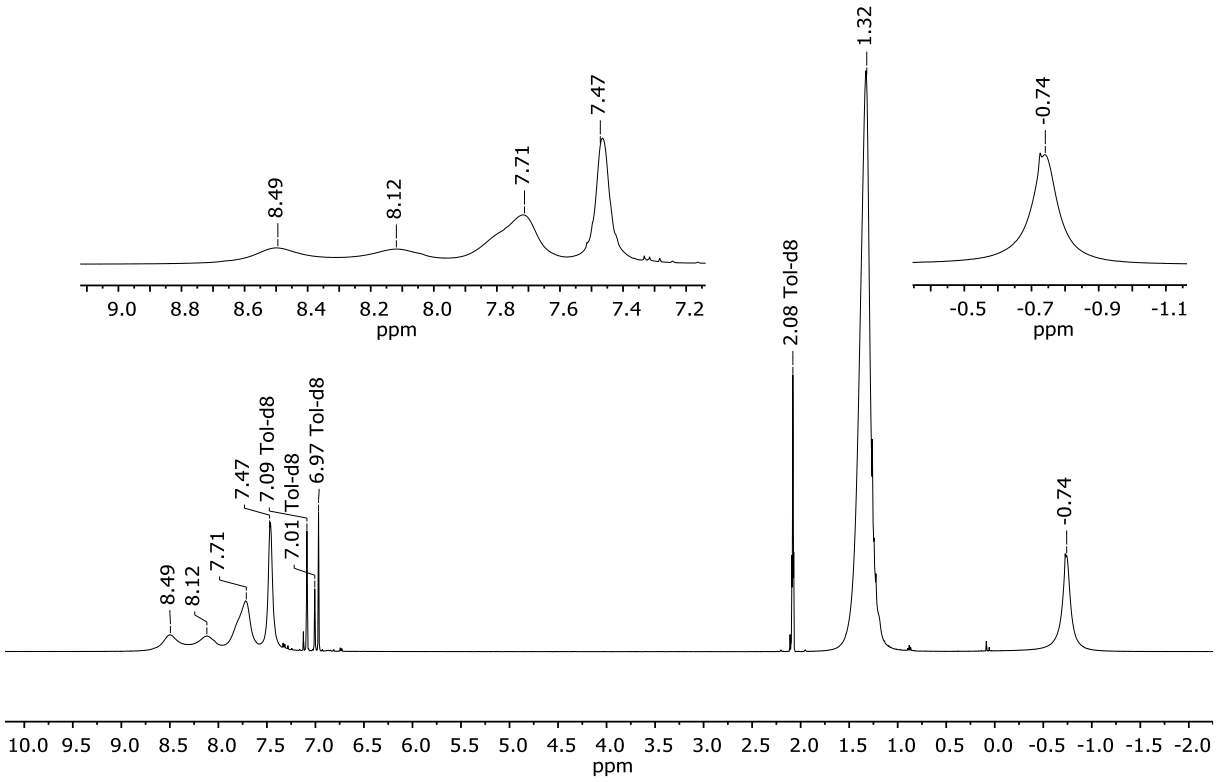

Fig. S7: ^{1}H NMR spectrum of (**2**)$_2$ (500.2 MHz, Tol-d_8, room temperature).

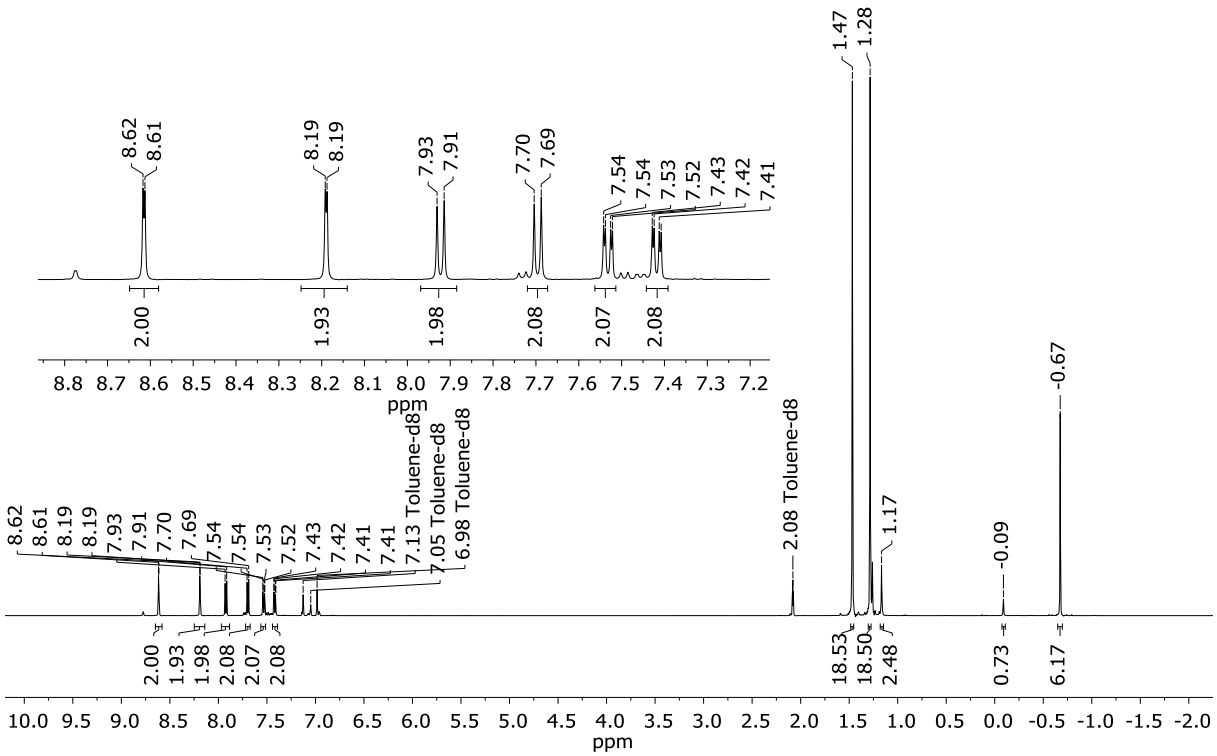

Fig. S8: ^{1}H NMR spectrum of (**2**)$_2$ (500.2 MHz, Tol-d_8, −30 °C). Major signals: *trans*-(**2**)$_2$; minor signals: *cis*-(**2**)$_2$.

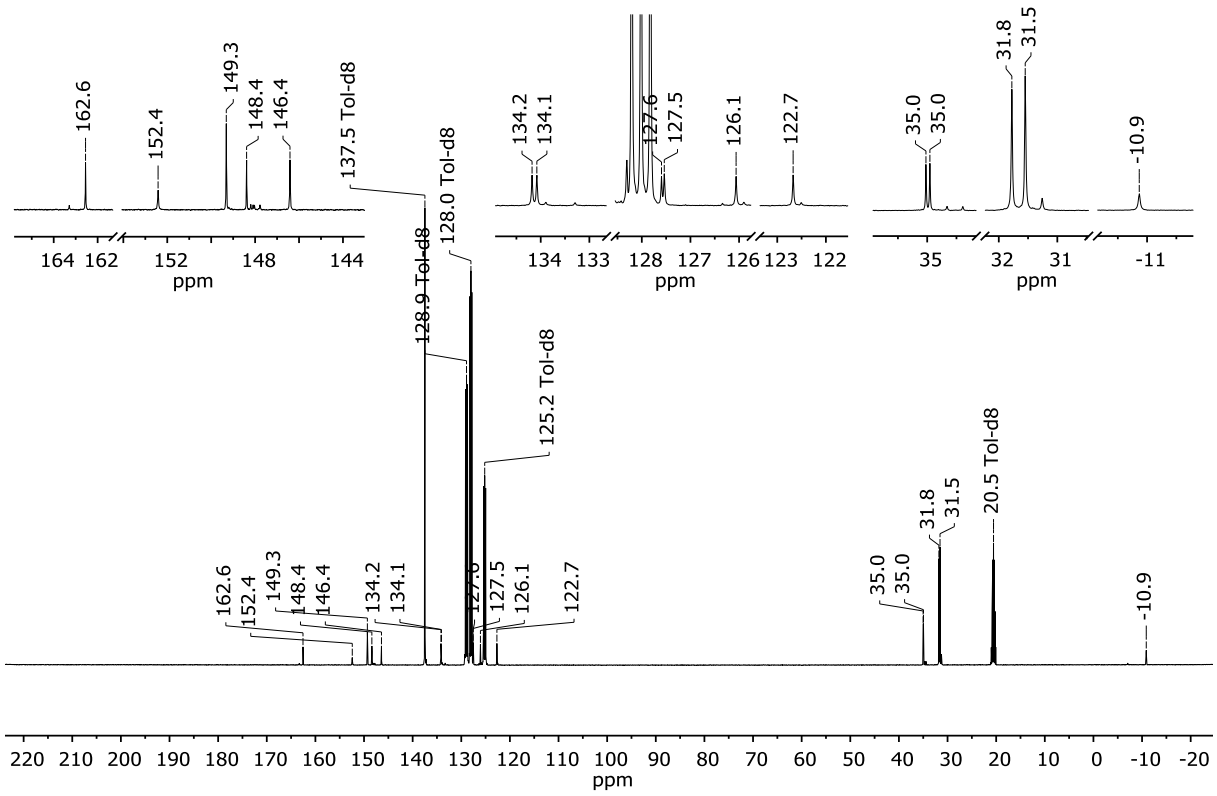

Fig. S9: $^{13}C\{^{1}H\}$ NMR spectrum of $(\mathbf{2})_2$ (125.8 MHz, Tol-d_8, −30 °C). Major signals: *trans*-$(\mathbf{2})_2$; minor signals: *cis*-$(\mathbf{2})_2$.

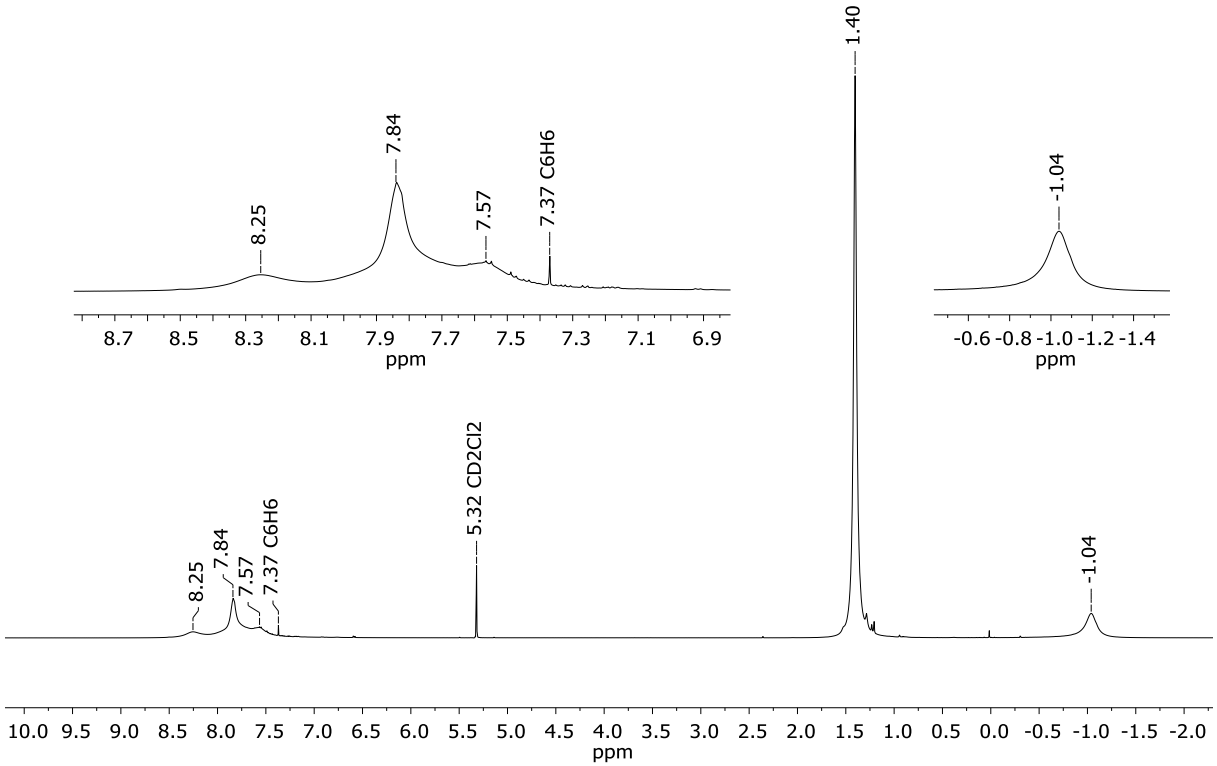

Fig. S10: ^{1}H NMR spectrum of $(\mathbf{2})_2$ (500.2 MHz, CD_2Cl_2, room temperature).

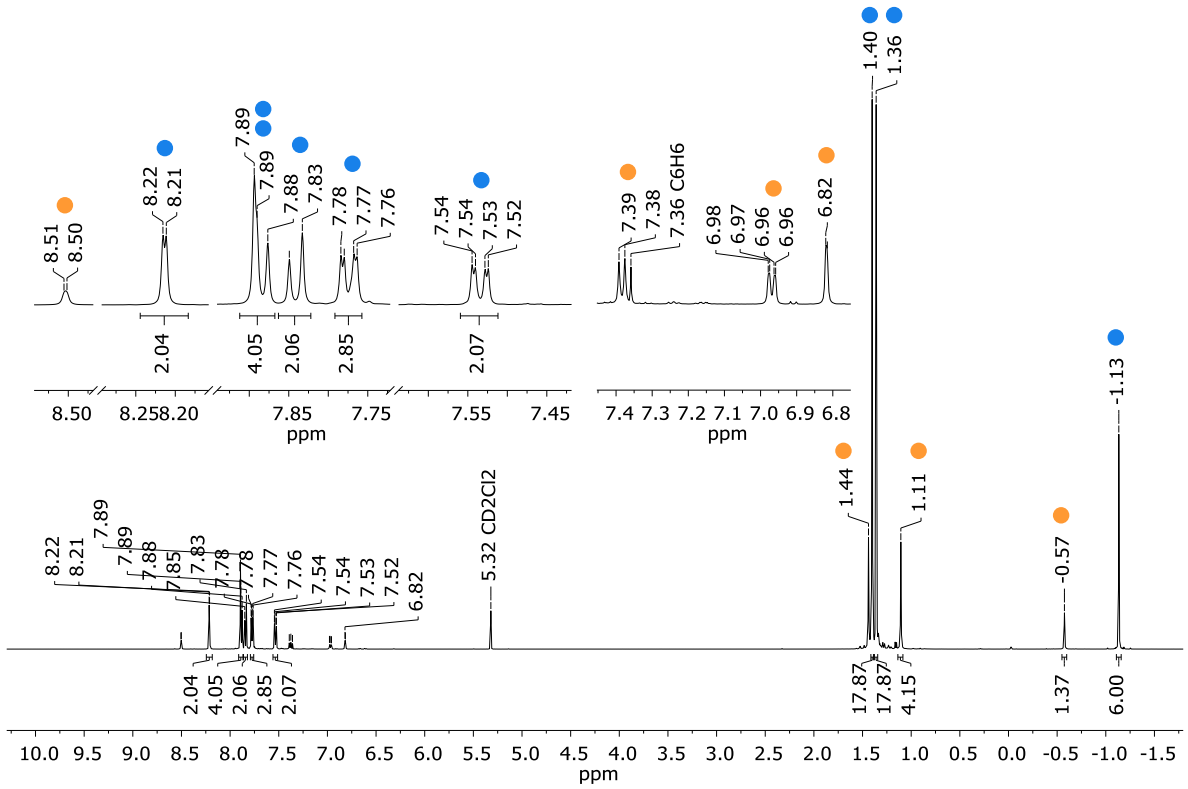

Fig. S11: ^{1}H NMR spectrum of (**2**)$_2$ (500.2 MHz, CD_2Cl_2, −30 °C). (● : *trans*-(**2**)$_2$; ● : *cis*-(**2**)$_2$).

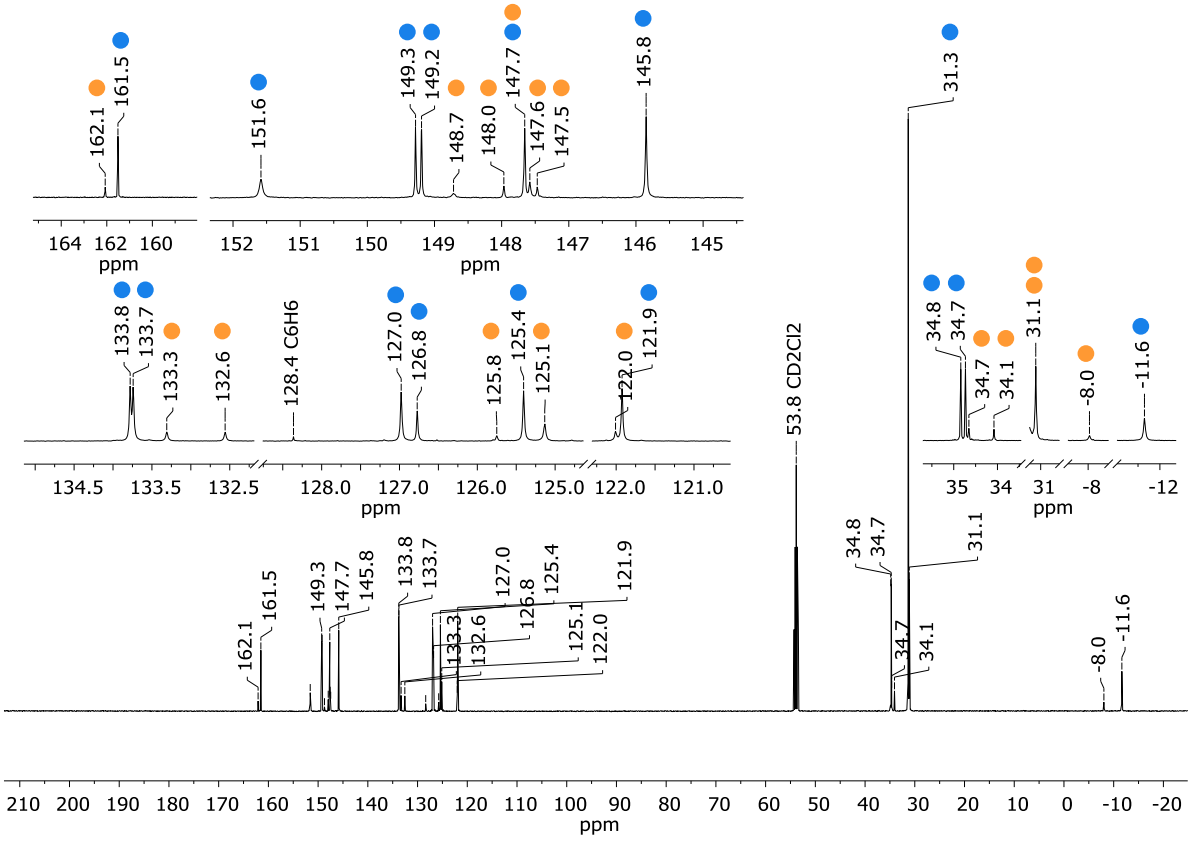

Fig. S12: $^{13}C\{^{1}H\}$ NMR spectrum of (**2**)$_2$ (125.8 MHz, CD_2Cl_2, −30 °C). (● : *trans*-(**2**)$_2$; ● : *cis*-(**2**)$_2$).

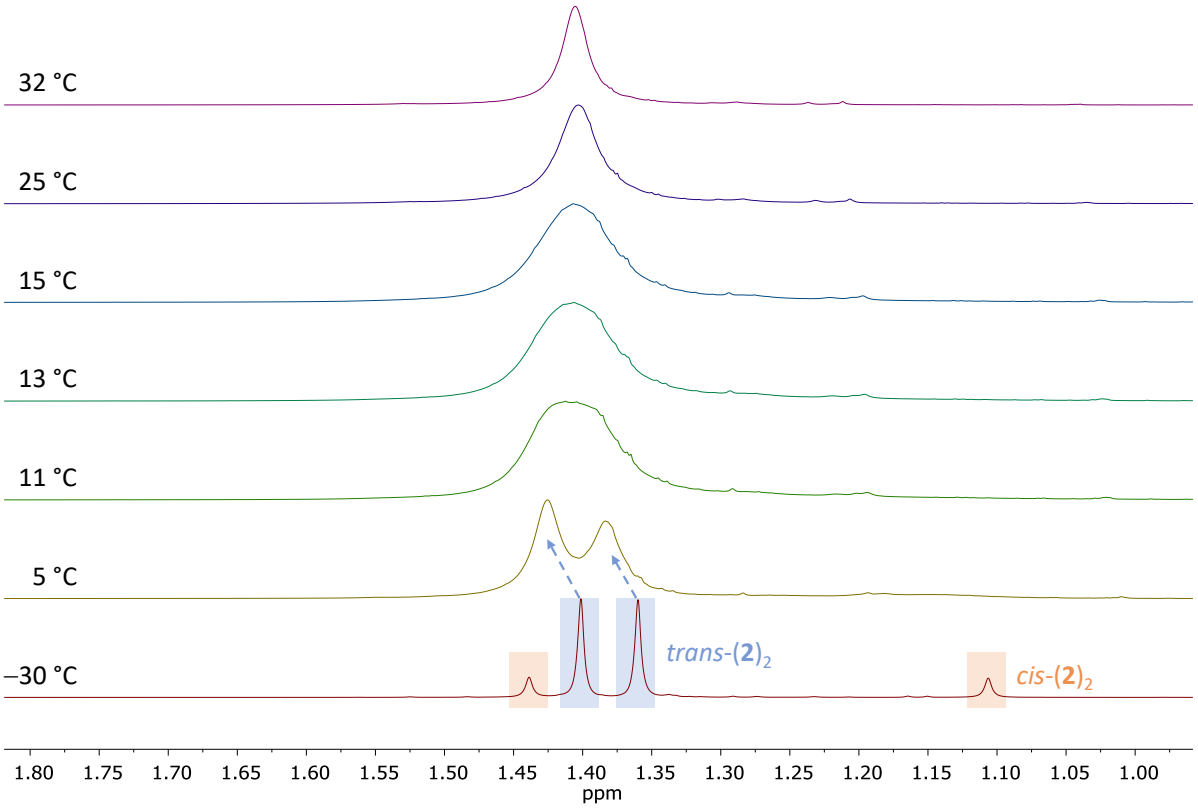

Fig. S13: Overlay of the ^{1}H NMR spectra of (**2**)$_2$ at different temperatures (500.2 MHz, CD_2Cl_2; *t*Bu resonances only). *Note*: The small change in the chemical shift values is due to the different measurement temperatures.

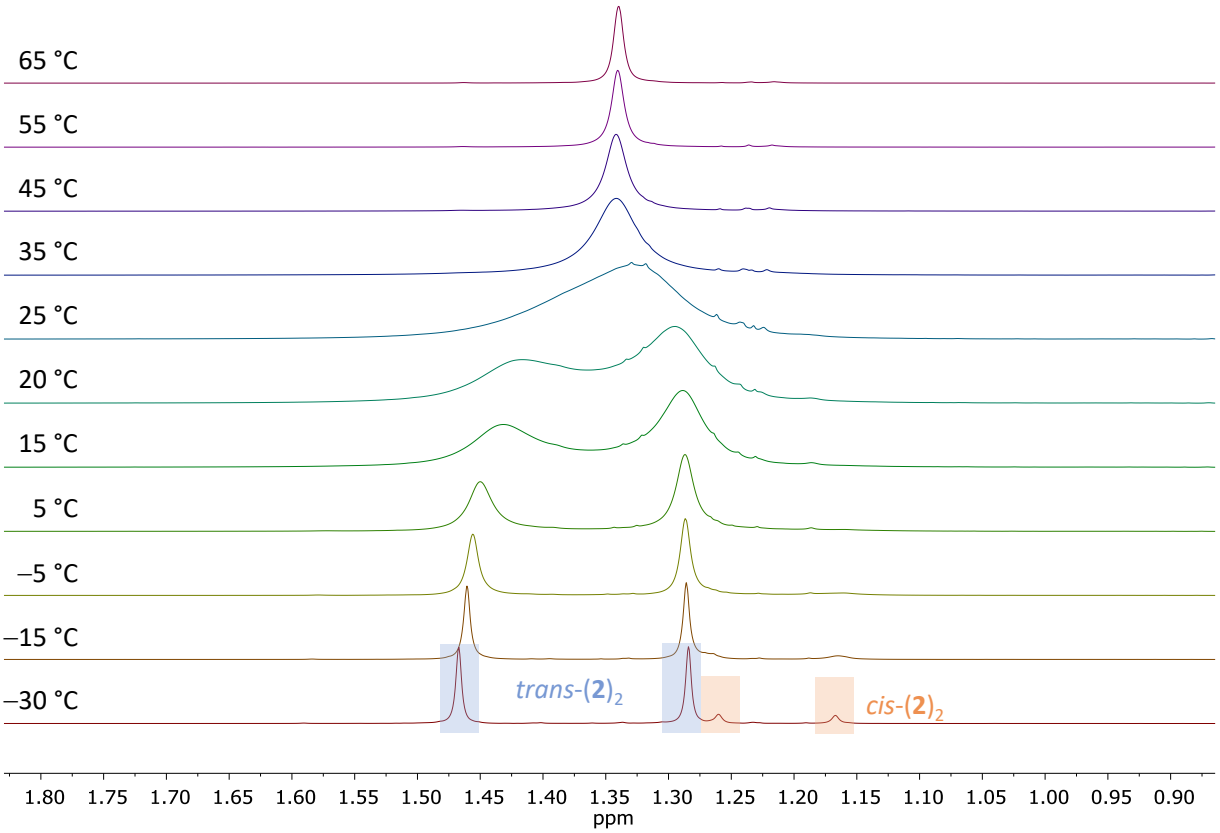

Fig. S14: Overlay of the ^{1}H NMR spectra of (**2**)$_2$ at different temperatures (500.2 MHz, Tol-d_8; *t*Bu resonances only). *Note*: The small change in the chemical shift values is due to the different measurement temperatures.

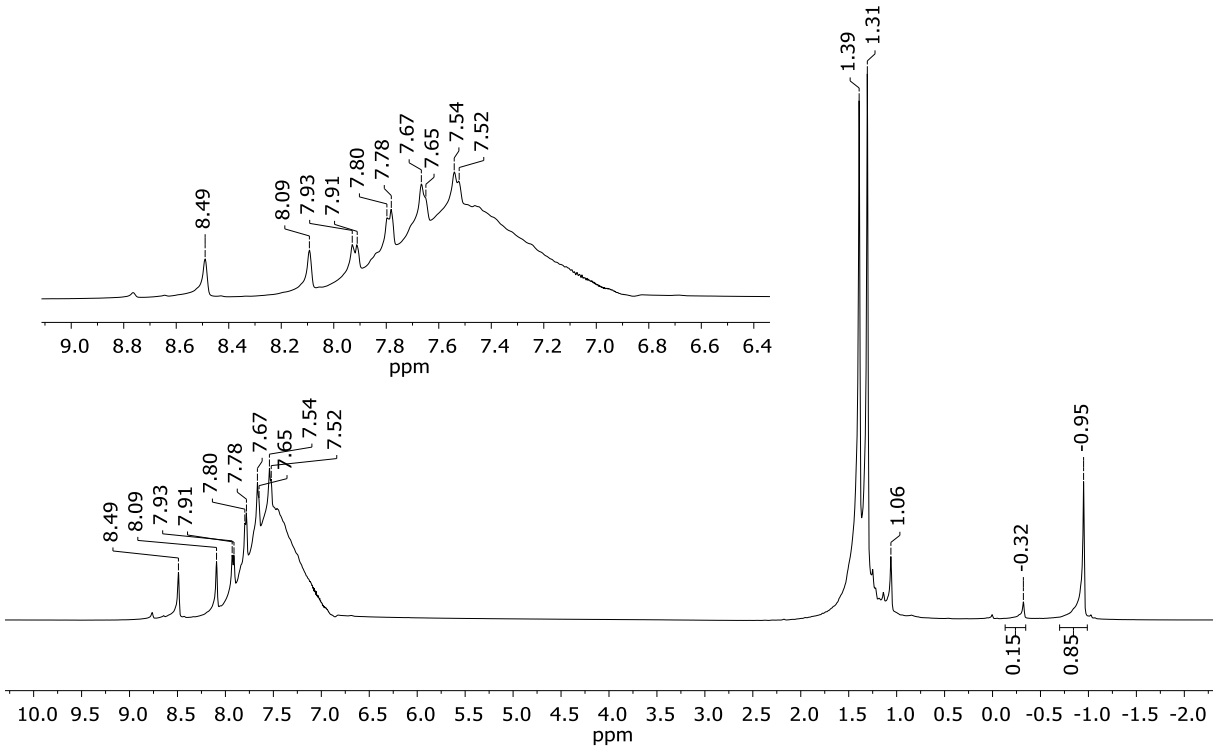

Fig. S15: ^{1}H NMR spectrum of (**2**)$_2$ (500.2 MHz, *o*DFB, −30 °C). *Note*: Only the integrals relevant for Chapter 1.4 are given. *Note*: The broad hump in the aromatic region is due to $C_6H_4F_2$ (*o*DFB).

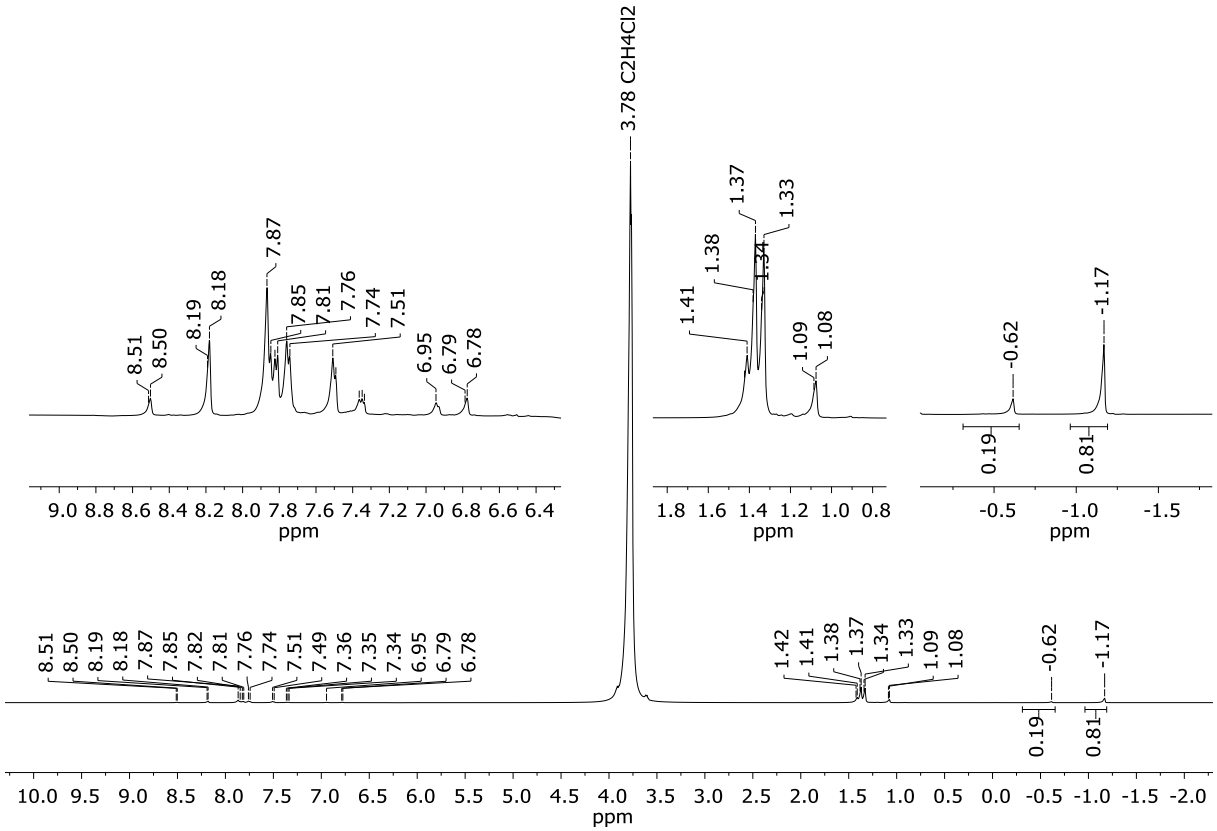

Fig. S16: ^{1}H NMR spectrum of (**2**)$_2$ (500.2 MHz, $C_2H_4Cl_2$, −30 °C). *Note*: Only the integrals relevant for Chapter 1.4 are given.

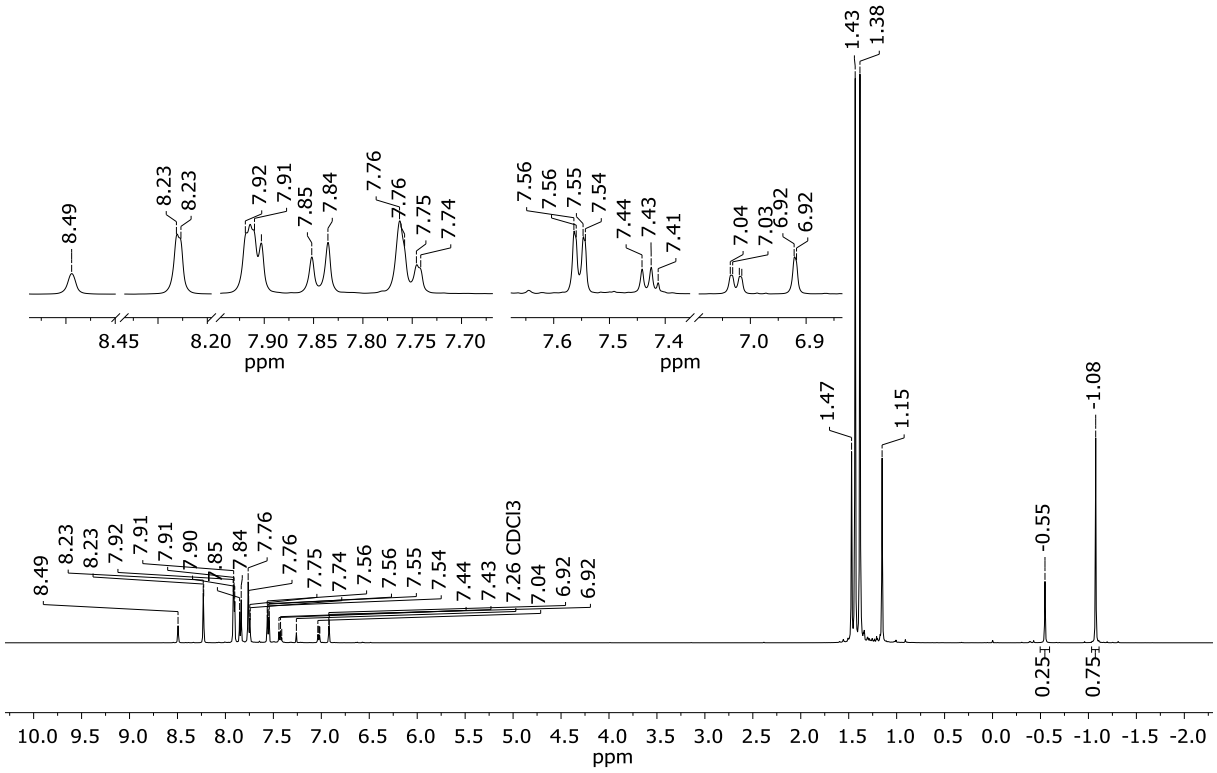

Fig. S17: ^{1}H NMR spectrum of (**2**)$_2$ (500.2 MHz, $CDCl_3$, −30 °C). *Note*: Only the integrals relevant for Chapter 1.4 are given.

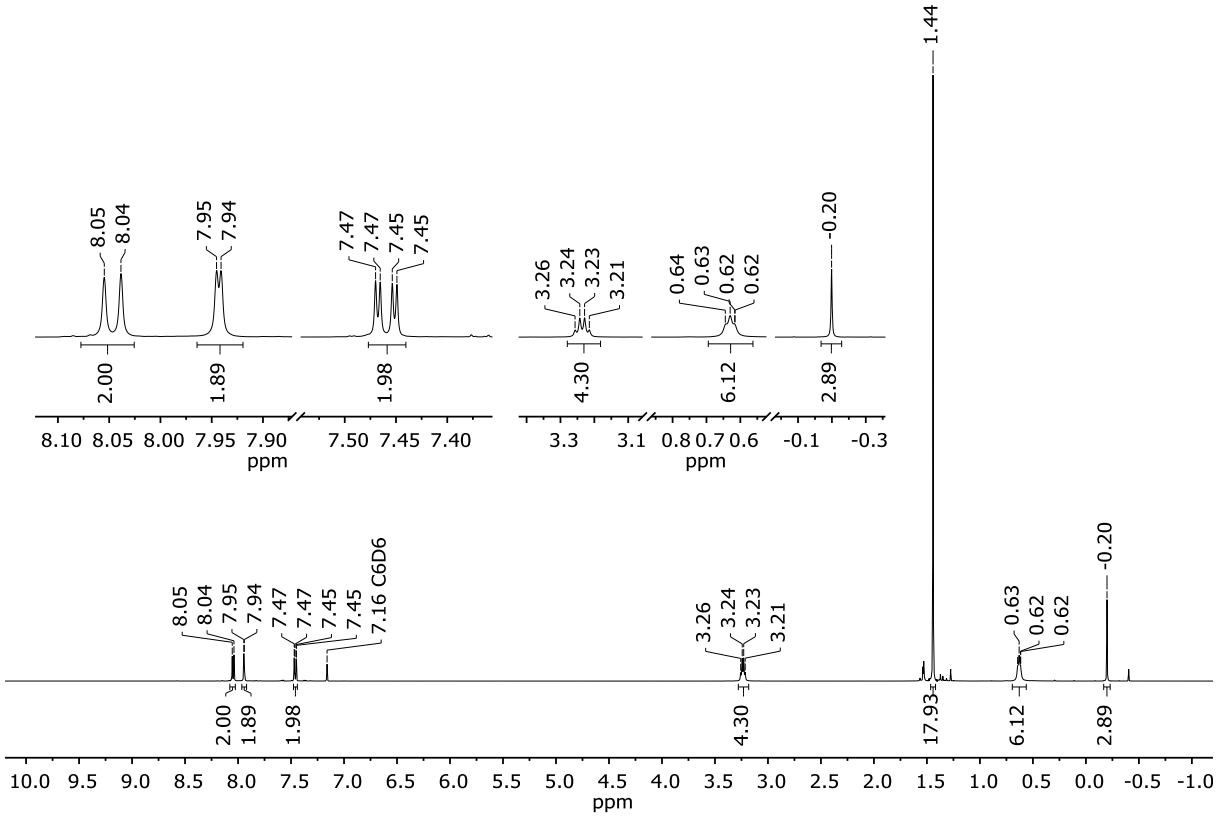

Fig. S18: ^{1}H NMR spectrum of **2**·OEt_2 (500.2 MHz, C_6D_6).

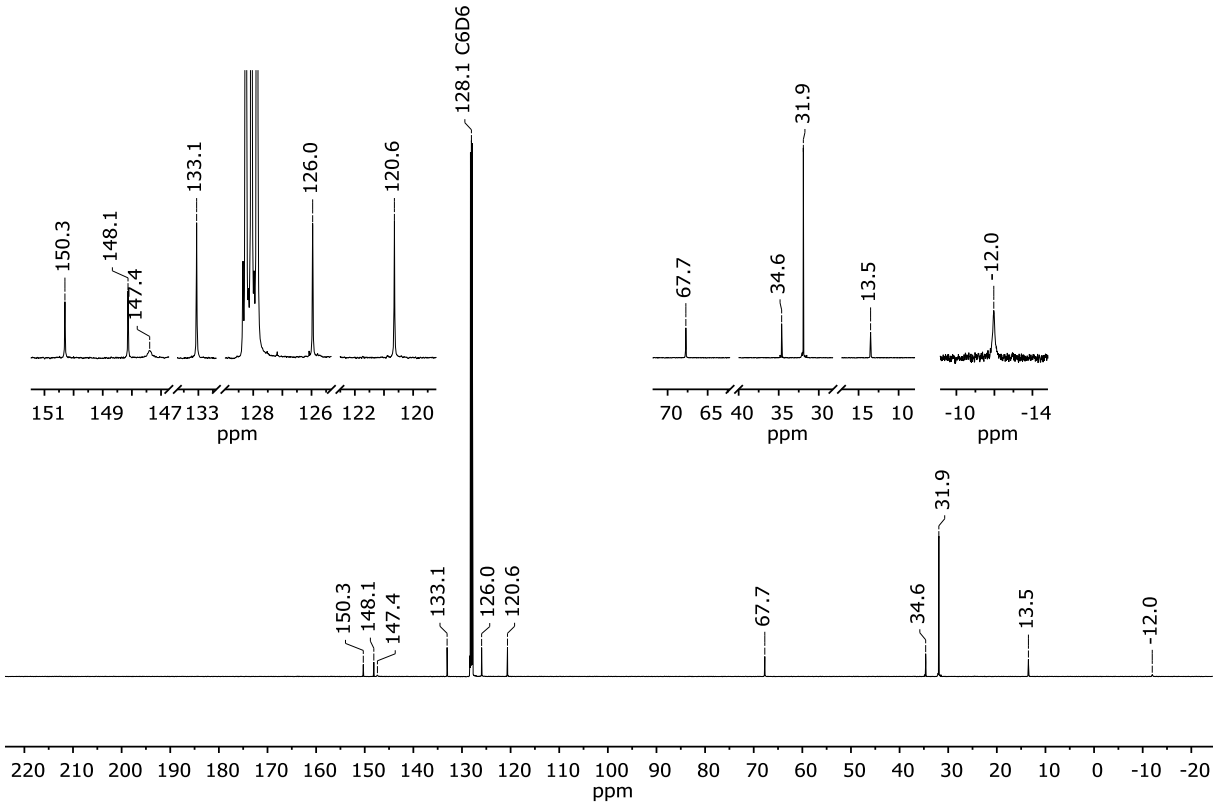

Fig. S19: $^{13}C\{^{1}H\}$ NMR spectrum of **2**·OEt_2 (125.8 MHz, C_6D_6).

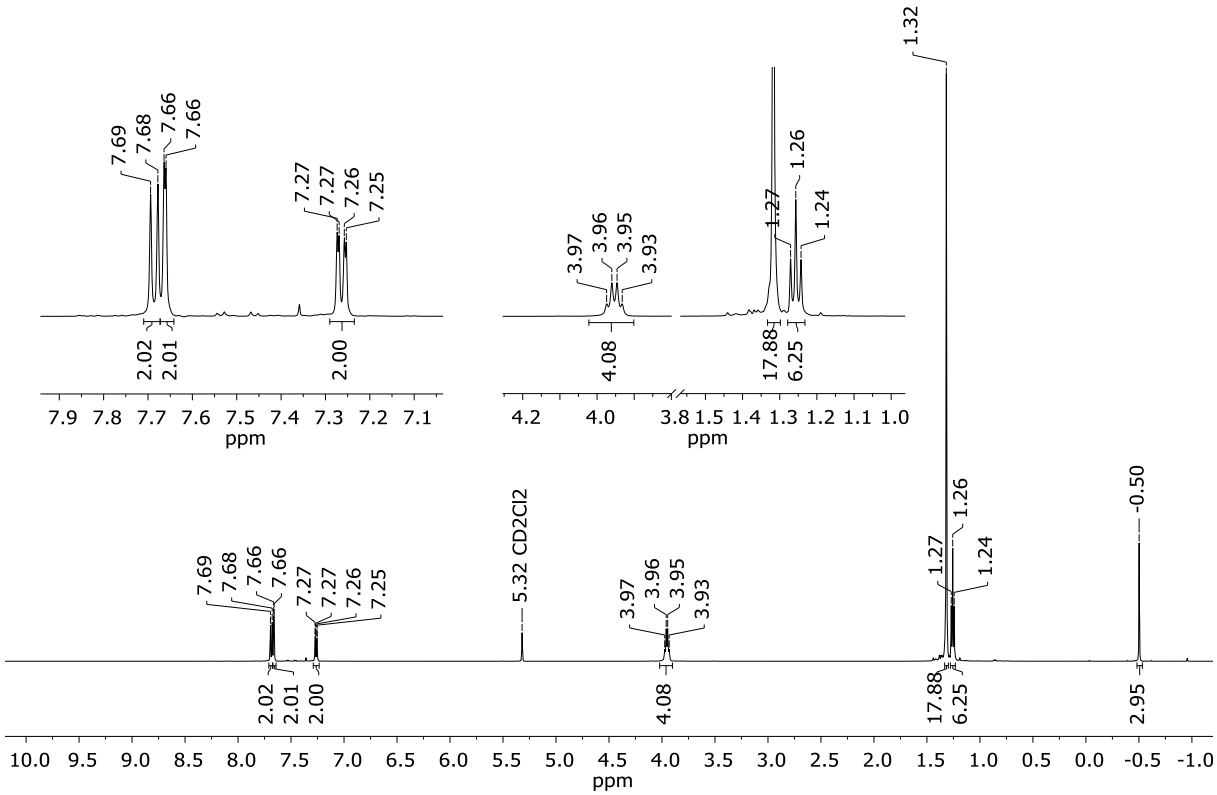

Fig. S20: ^{1}H NMR spectrum of **2**·OEt_2 (500.2 MHz, CD_2Cl_2, –30 °C).

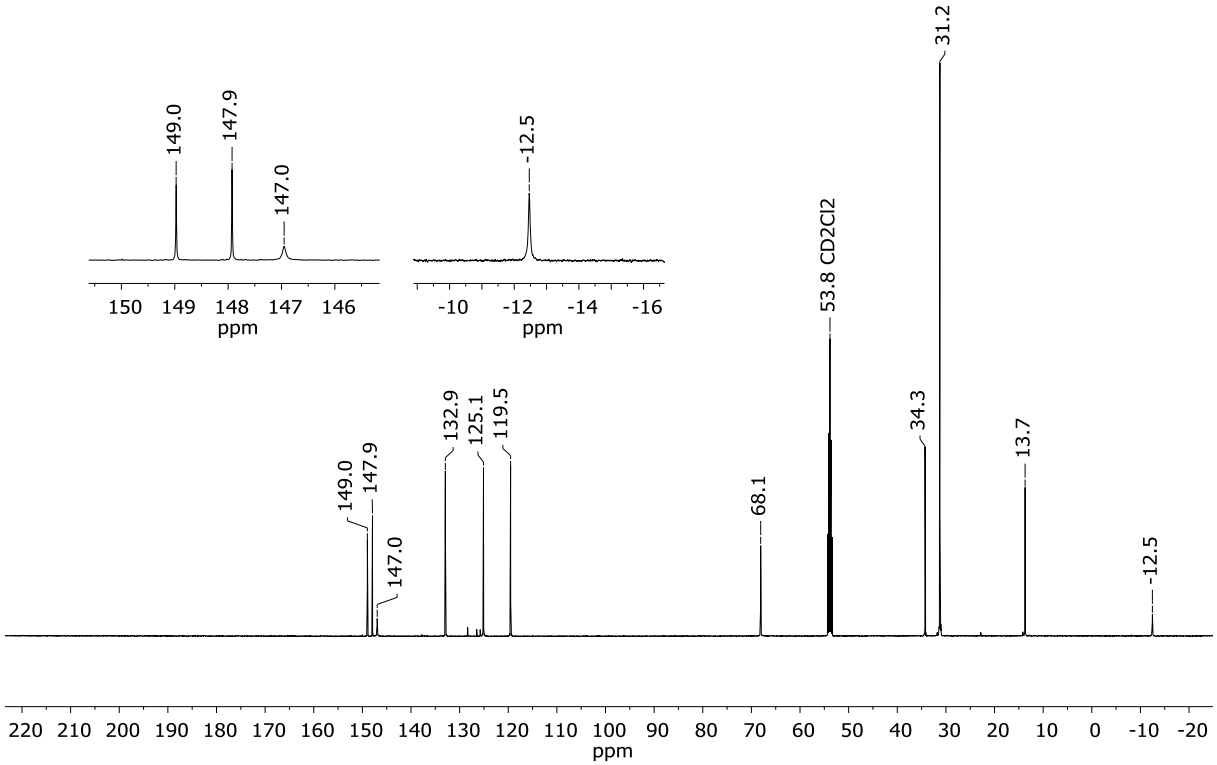

Fig. S21: $^{13}C\{^{1}H\}$ NMR spectrum of **2**·OEt_2 (125.8 MHz, CD_2Cl_2, –30 °C). *Note*: The minor signals are assignable to toluene originating from the starting material $(\mathbf{2})_2$.

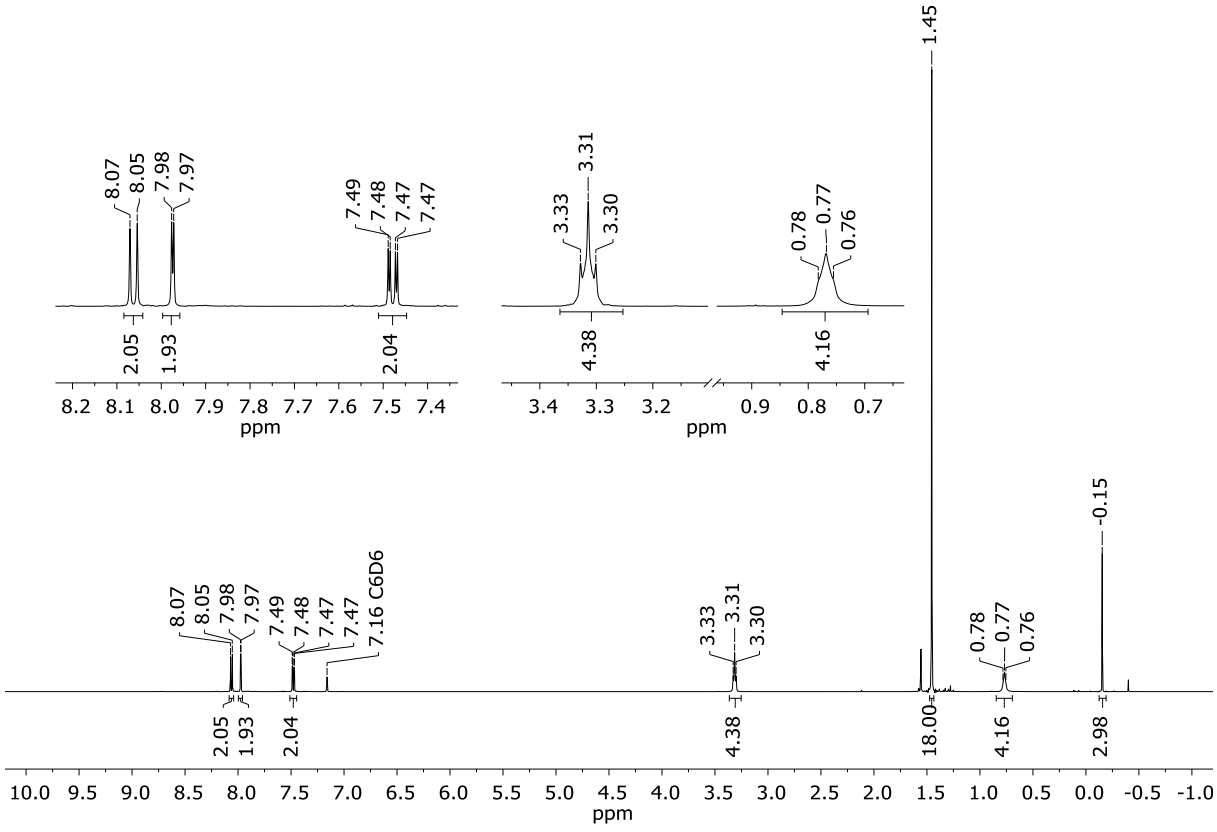

Fig. S22: ^{1}H NMR spectrum of **2**·thf (500.2 MHz, C_6D_6).

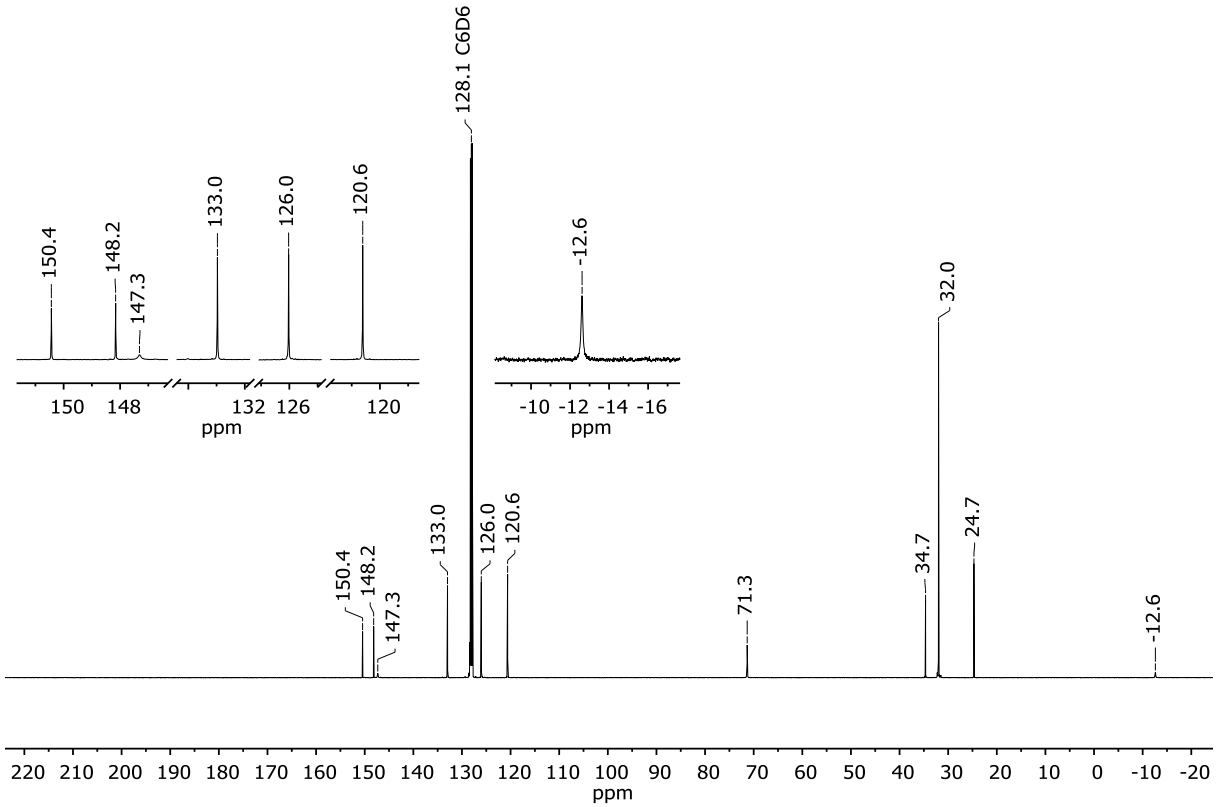

Fig. S23: $^{13}C\{^{1}H\}$ NMR spectrum of **2**·thf (125.8 MHz, C_6D_6).

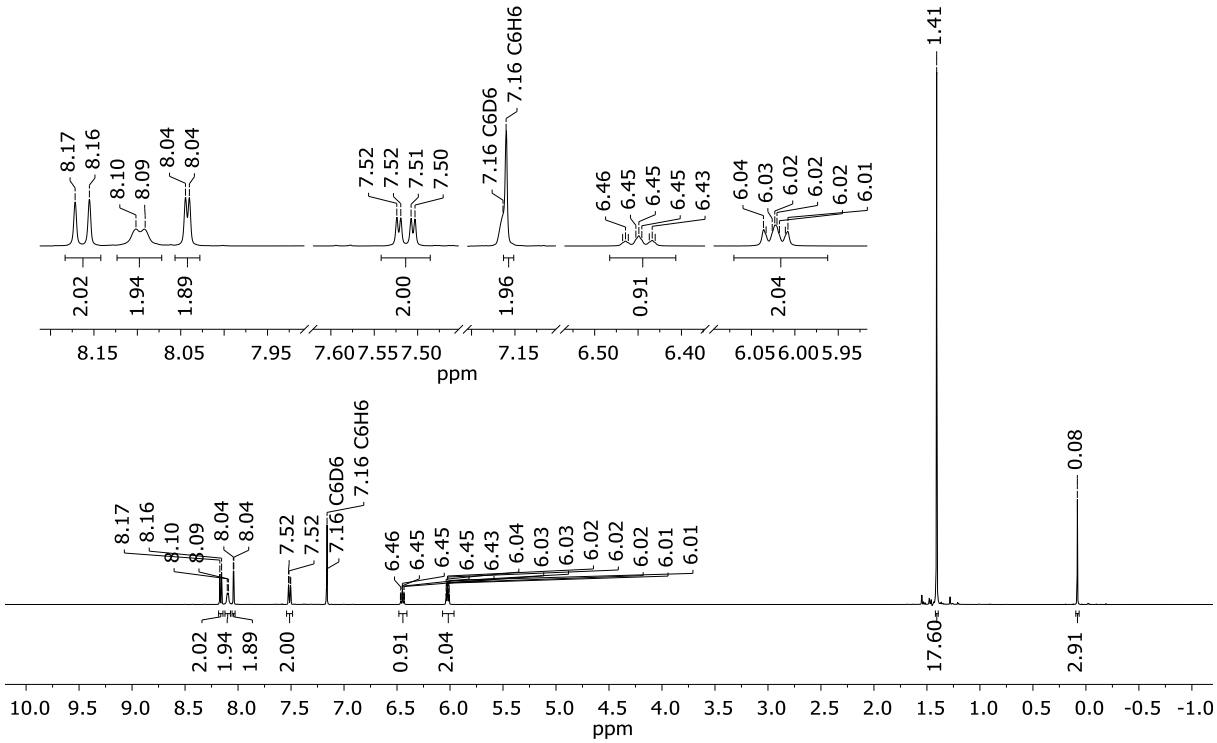

Fig. S24: ^{1}H NMR spectrum of **2**·py (500.2 MHz, C_6D_6).

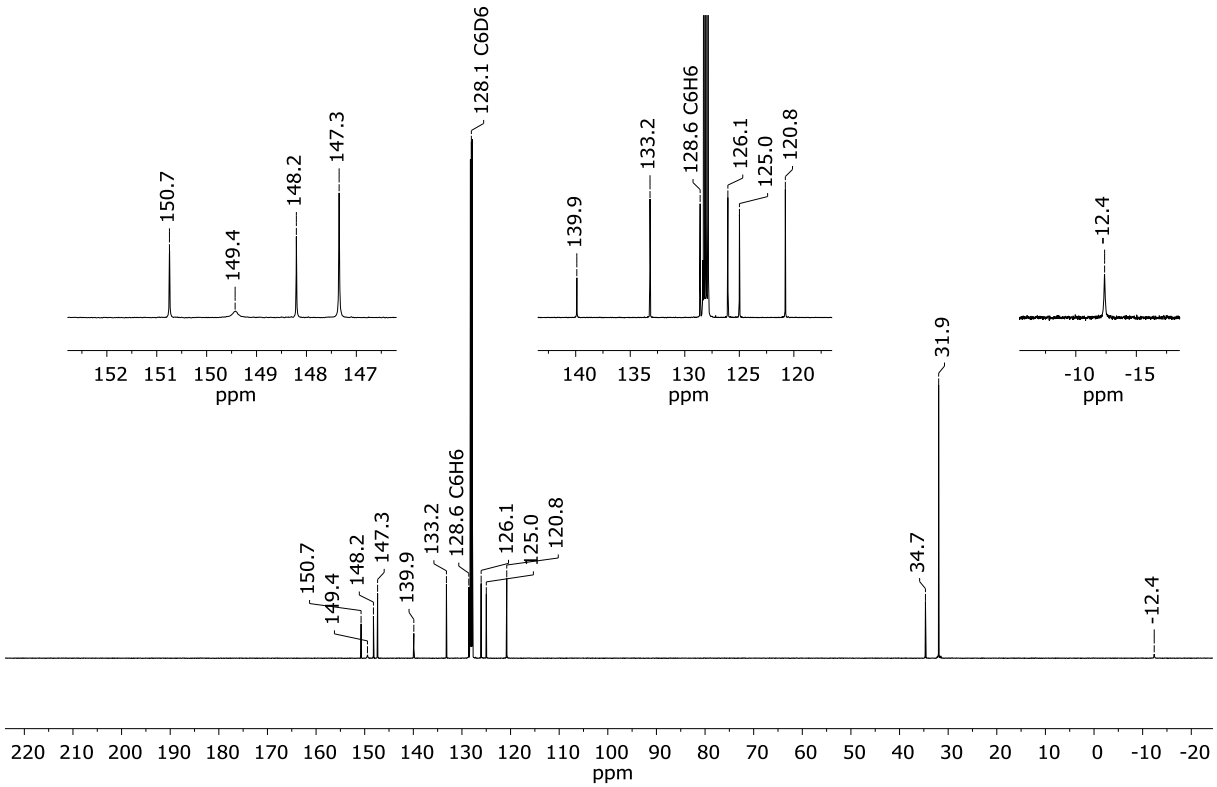

Fig. S25: $^{13}C\{^{1}H\}$ NMR spectrum of **2**·py (125.8 MHz, C_6D_6).

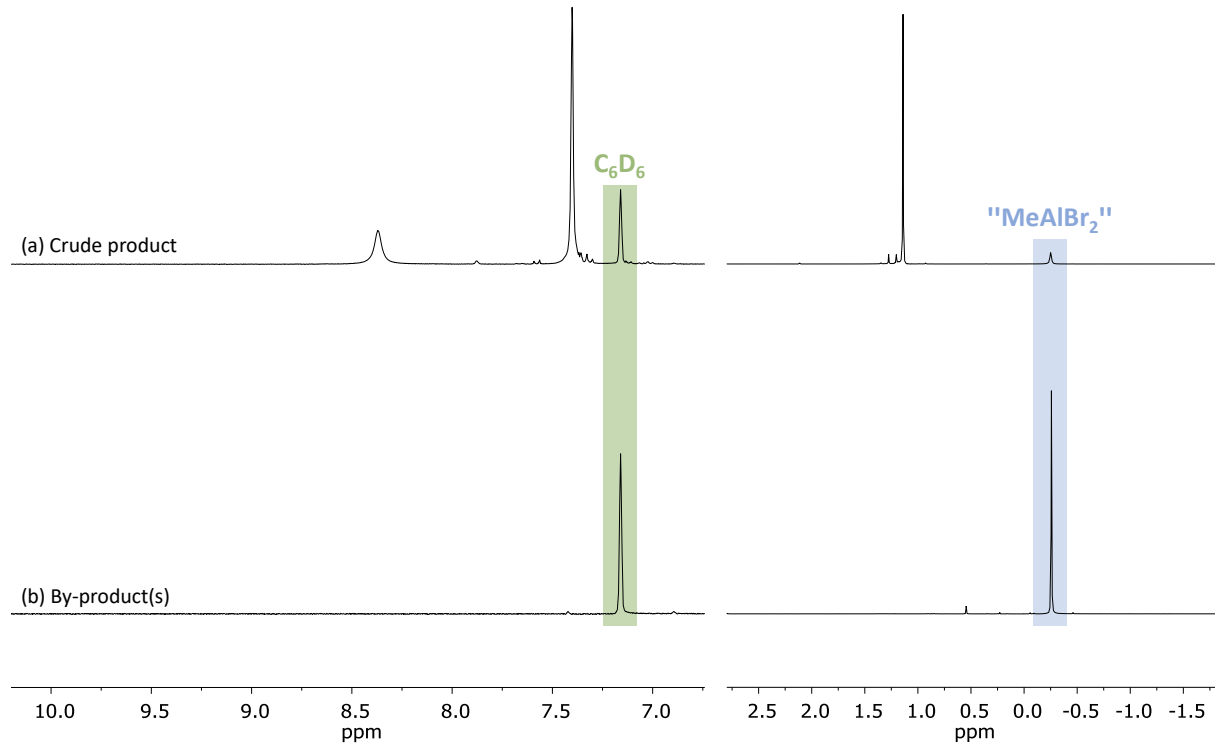

Fig. S26: ^{1}H NMR spectra of (a) the crude product obtained from the reaction of $(\mathbf{2})_2$ with $AlBr_3$ and (b) the by-product(s) that could be sublimed off under vacuum at high temperature (300.0 MHz, C_6D_6). *Note*: The intensities of the signals in the aliphatic vs. the aromatic region are not to scale; the spectrum of the purified sample is shown in Fig. S27.

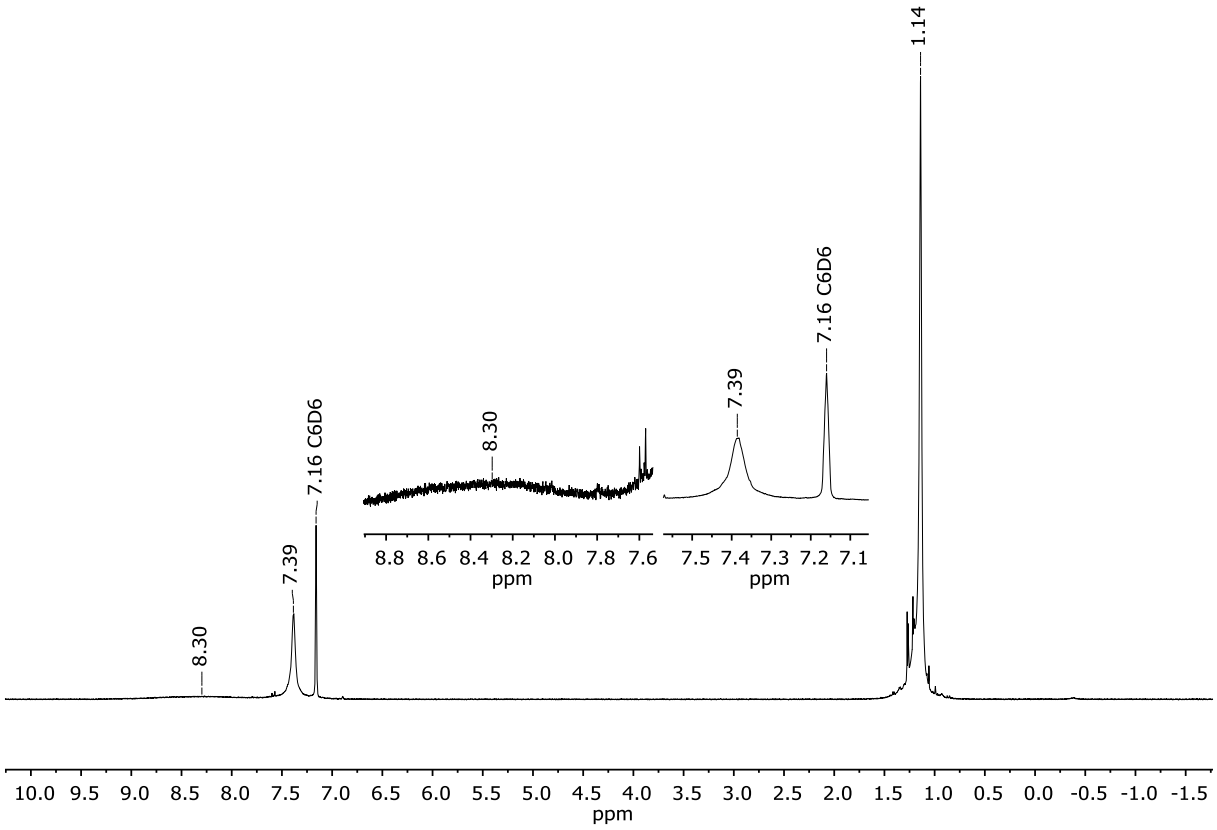

Fig. S27: ^{1}H NMR spectrum of (**3**)$_2$ (500.2 MHz, C_6D_6).

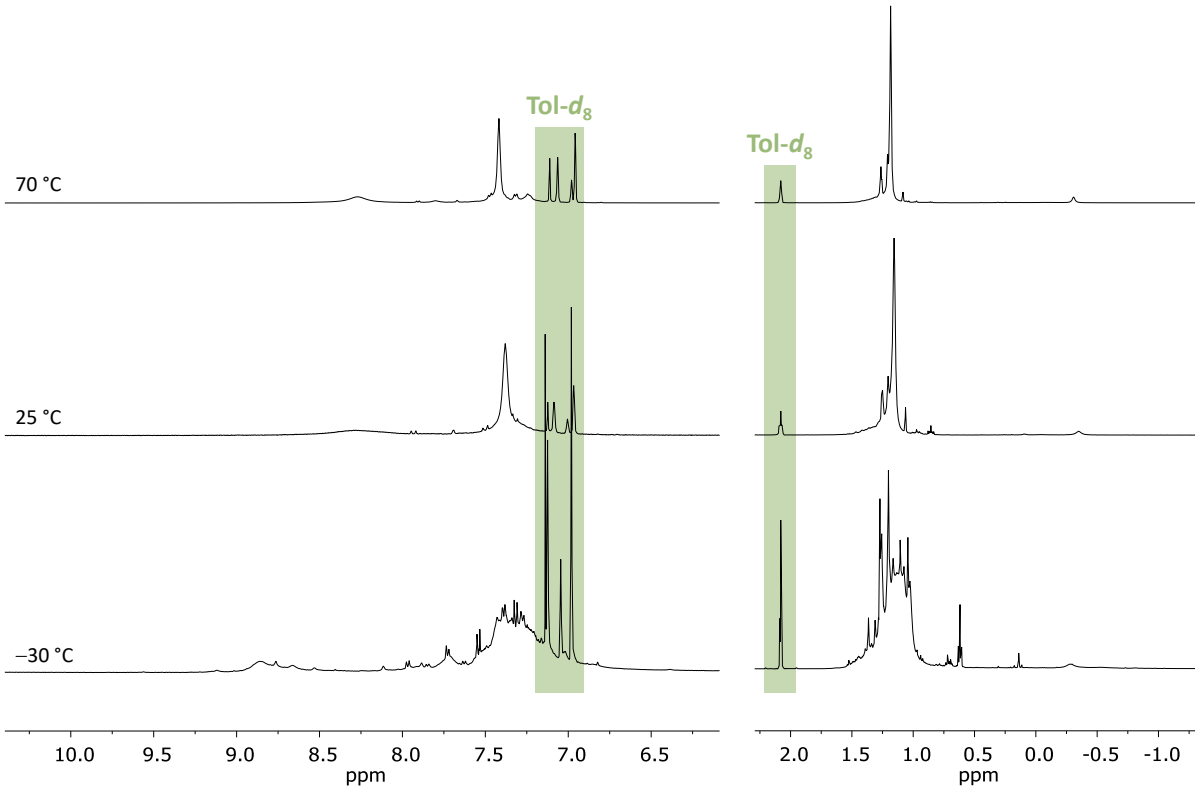

Fig. S28: ^{1}H NMR spectra of (**3**)$_2$ (500.2 MHz, C_6D_6, different temperatures). *Note*: The intensities of the signals in the aliphatic vs. the aromatic region are not to scale.

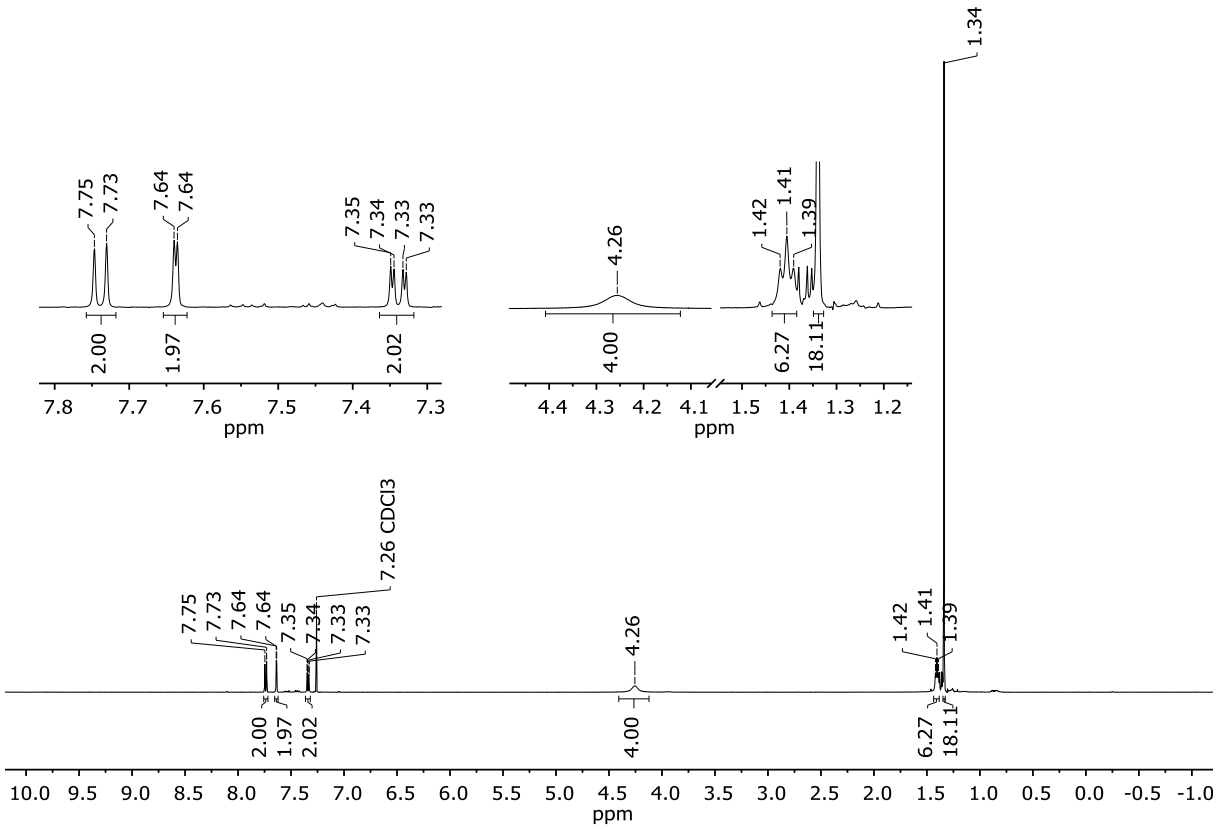

Fig. S29: ^{1}H NMR spectrum of **4**·OEt_2 (500.2 MHz, $CDCl_3$).

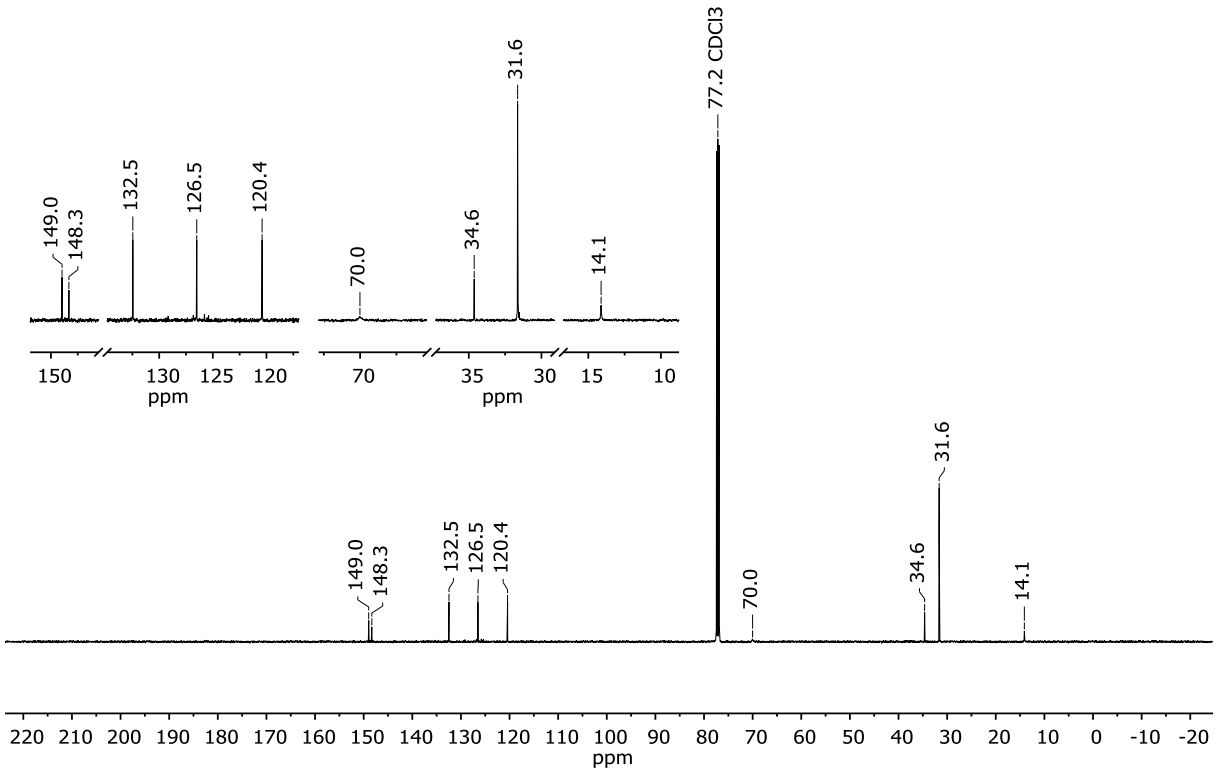

Fig. S30: $^{13}C\{^{1}H\}$ NMR spectrum of **4**·OEt_2 (125.8 MHz, $CDCl_3$).

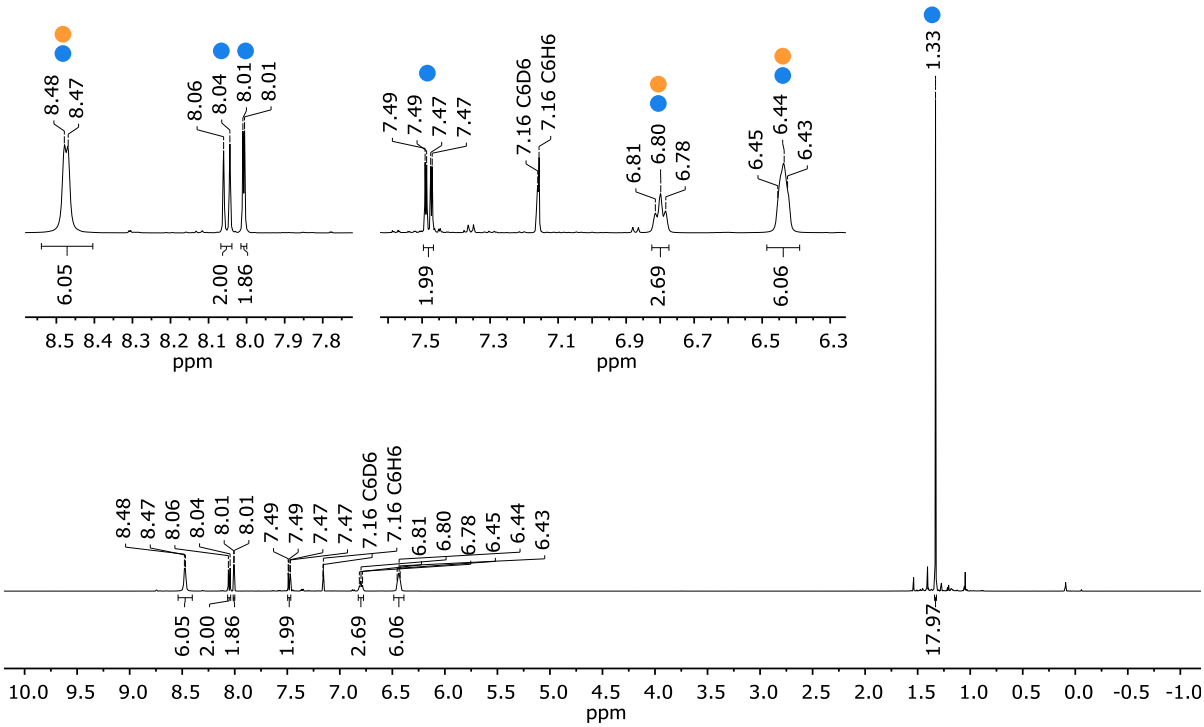

Fig. S31: ^{1}H NMR spectrum (500.2 MHz, C_6D_6) recorded on the reaction mixture of **3** and py. (● : **4**·py; ● : **5**)

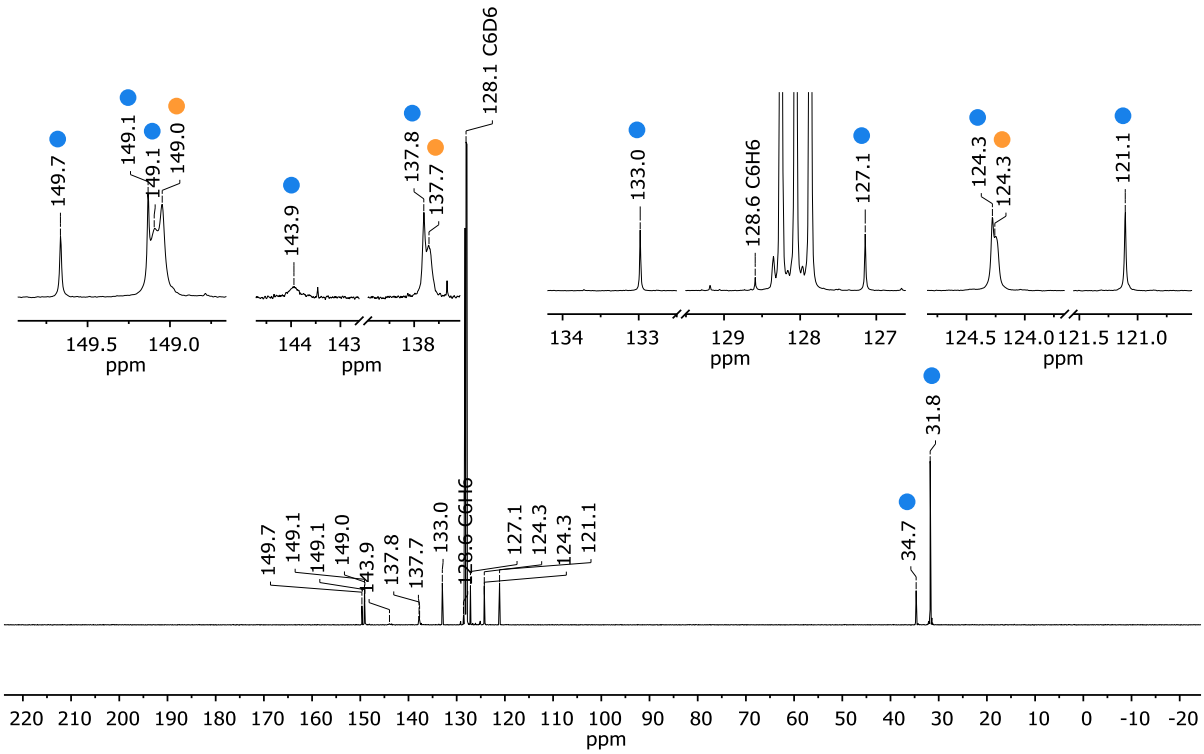

Fig. S32: $^{13}C\{^{1}H\}$ NMR spectrum (125.8 M3Hz, C_6D_6) recorded on the reaction mixture of **3** and py. (● : **4**·py; ● : **5**)

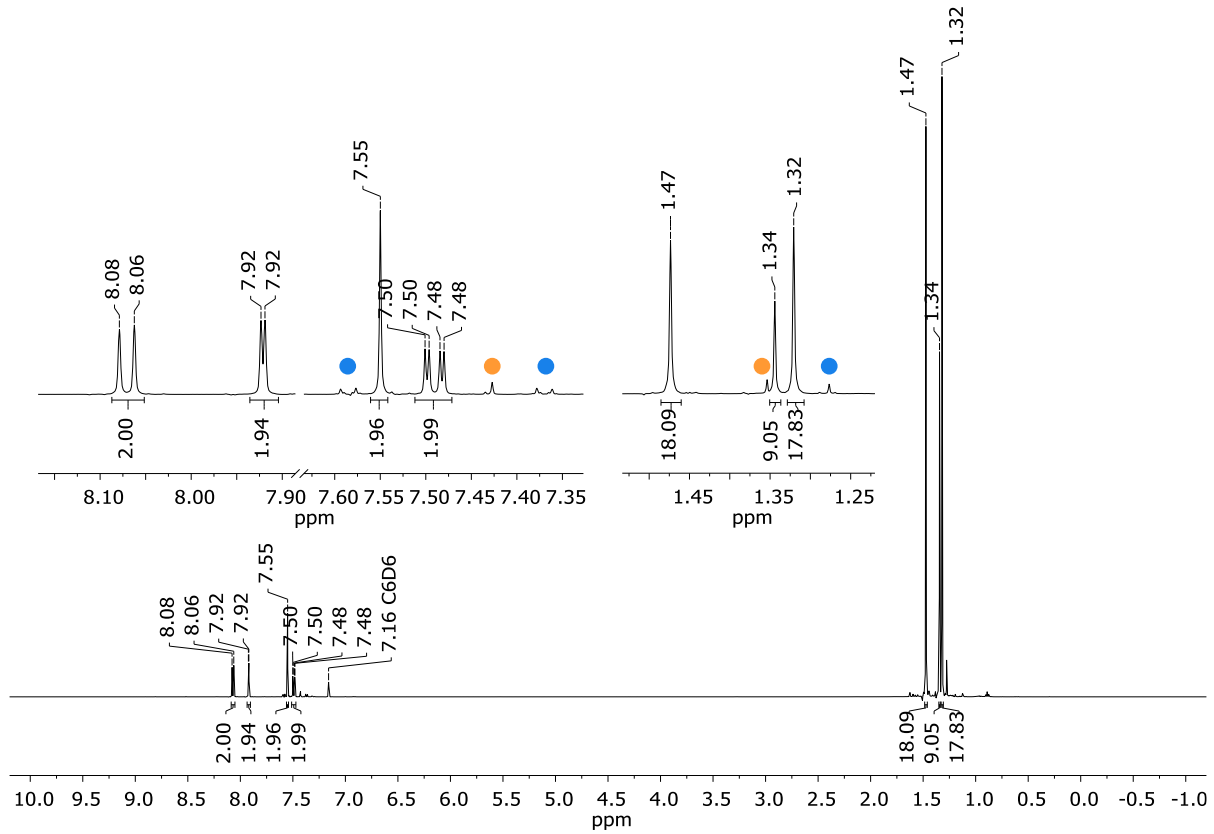

Fig. S33: ^{1}H NMR spectrum of **6** (500.2 MHz, C_6D_6). Observed minor components: 4,4'-Di-*tert*-butylbiphenyl (●), Mes*H (●).

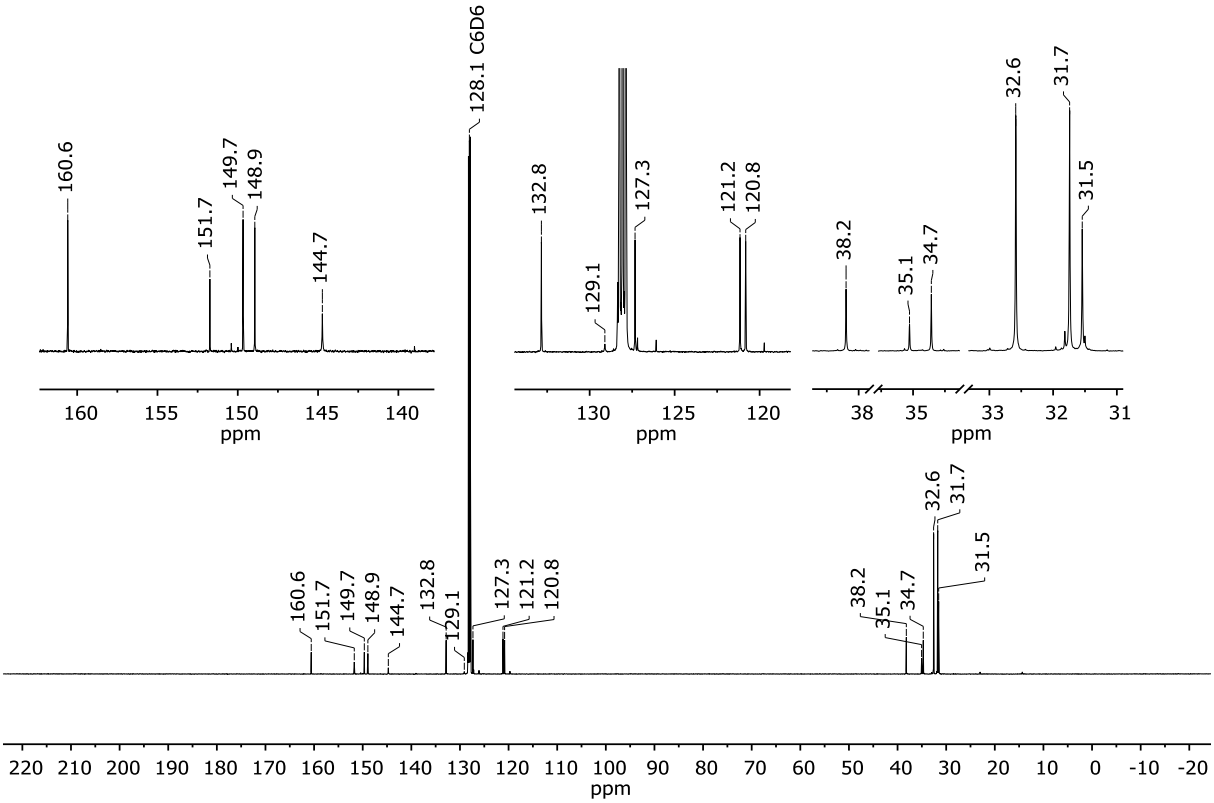

Fig. S34: $^{13}C\{^{1}H\}$ NMR spectrum of **6** (125.8 MHz, C_6D_6). *Note*: The observed minor components 4,4'-di-*tert*-butylbiphenyl and Mes*H were not marked due to the low intensity of the signals.

3 Single-crystal X-ray structure analyses

Single-crystal diffraction data were collected at −100 °C on a *STOE IPDS II* two-circle diffractometer equipped with a *Genix 3D HS* microfocus MoK_α X-ray source (λ = 0.71073 Å). The finalization of the data, including empirical absorption corrections, was done using the *CrysAlisPro* software v.1.171.42.43a (*Rigaku Oxford Diffraction*, 2022). The structures were solved using the *SHELXS* and *SHELXT* programs and refined against $|F|^2$ with full-matrix least-squares techniques using the program *SHELXL*-2018/3.[S10–S12] All H atoms were located geometrically and refined riding on the pivot atom.

Topological aspects of the packing of molecules in crystals were analyzed with the *TOPOS 4.0 Professional* (*ToposPro*) program set.[S13]

CIF files containing the crystallographic information are deposited with the Cambridge Crystallographic Data Center under the deposition codes CSD2394332-2394341 and can be obtained free of charge via www.ccdc.cam.ac.uk/data_request/cif. Crystallographic data and parameters of the diffraction experiments are given in Tables S2-S7.

Table S2: Selected crystallographic data for **1**.

	1
Chemical formula	$C_{22}H_{30}Sn$
M_r	413.15
Crystal system, space group	Triclinic, $P\bar{1}$
Temperature (K)	173
a, b, c (Å)	9.0724(5), 9.1851(5), 13.8604(7)
α, β, γ (°)	88.933(4), 78.708(4), 63.108(6)
V (Å^3)	1006.92(10)
Z	2
F(000)	424
D_x (Mg m^{-3})	1.363
Radiation type	Mo $K\alpha$
μ (mm^{-1})	1.27
Crystal shape	Block
Color	Colorless
Crystal size (mm)	0.24 × 0.18 × 0.16
Absorption correction	Multi-scan
T_{min}, T_{max}	0.573, 1.000
No. of measured, independent and observed [$I > 2s(I)$] reflections	20383, 3958, 3707
R_{int}	0.042
Θ_{max} (°)	26.0
Range of h, k, l	h = −11→11, k = −11→11, l = −16→17
$R[F^2 > 2s(F^2)]$, $wR(F^2)$, S	0.032, 0.079, 1.14
No. of reflections	3958
No. of parameters	216
$\Delta\rho_{max}$, $\Delta\rho_{min}$ (e Å^{-3})	1.27, −0.72

Computer programs: *X-AREA* (*Stoe & Cie*, 2001), *CrysAlis PRO* 1.171.42.43a (*Rigaku OD*, 2022), *SHELXS* (G. M. Sheldrick, 1997), *SHELXT* (G. M. Sheldrick, 2015), *SHELXL-2018*/3 (Sheldrick, 2018).

Table S3: Selected crystallographic data for α-*trans*-(**2**)$_2$ and β-*trans*-(**2**)$_2$.

	α-*trans*-(**2**)$_2$	β-*trans*-(**2**)$_2$
Chemical formula	$C_{42}H_{54}Al_2$	$C_{42}H_{54}Al_2$
M_r	612.81	612.81
Crystal system, space group	Triclinic, $P\bar{1}$	Monoclinic, $P2_1/n$
Temperature (K)	173	173
a, b, c (Å)	13.1587(8), 14.9947(10), 15.6441(9)	9.2544(11), 12.0149(11), 17.0828(17)
α, β, γ (°)	73.852(5), 71.308(5), 88.245(5)	90, 90.972(10), 90
V (Å^3)	2802.8(3)	1899.2(3)
Z	3	2
F(000)	996	664
D_x (Mg m^{-3})	1.089	1.072
Radiation type	Mo $K\alpha$	Mo $K\alpha$
μ (mm^{-1})	0.10	0.10
Crystal shape	Plate	Block
Color	Colorless	Colorless
Crystal size (mm)	0.61 × 0.51 × 0.09	0.29 × 0.29 × 0.28
Absorption correction	Multi-scan	Multi-scan
T_{min}, T_{max}	0.721, 1.000	0.773, 1.000
No. of measured, independent and observed [$I > 2s(I)$] reflections	27580, 10585, 8133	23747, 3608, 2611
R_{int}	0.059	0.092
Θ_{max} (°)	25.7	25.7
Range of h, k, l	h = −16→16, k = −15→18, l = −19→19	h = −10→11, k = −14→14, l = −20→20
$R[F^2 > 2s(F^2)]$, $wR(F^2)$, S	0.051, 0.144, 1.03	0.063, 0.173, 0.95
No. of reflections	10585	3608
No. of parameters	631	222
$\Delta\rho_{max}$, $\Delta\rho_{min}$ (e Å^{-3})	0.61, −0.30	0.38, −0.45

Computer programs: *X-AREA* (*Stoe & Cie*, 2001), *CrysAlis PRO* 1.171.42.43a (*Rigaku OD*, 2022), *SHELXS* (G. M. Sheldrick, 1997), *SHELXT* (G. M. Sheldrick, 2015), *SHELXL-2018*/3 (Sheldrick, 2018).

Table S4: Selected crystallographic data for **2**·OEt_2 and **2**·py × $(C_6H_6)_{0.5}$.

	2·OEt_2	**2**·py × $(C_6H_6)_{0.5}$
Chemical formula	$C_{25}H_{37}AlO$	$C_{26}H_{32}AlN \times (C_6H_6)_{0.5}$
M_r	380.52	424.56
Crystal system, space group	Monoclinic, *C*2/*c*	Monoclinic, $P2_1/n$
Temperature (K)	173	173
a, *b*, *c* (Å)	29.540(12), 7.650(4), 23.963(8)	16.4386(7), 18.5881(6), 18.6041(8)
α, β, γ (°)	90, 116.36(4), 90	90, 113.920(5), 90
V (Å^3)	4852(4)	5196.5(4)
Z	8	8
F(000)	1664	1832
D_x (Mg m^{-3})	1.042	1.085
Radiation type	Mo *K*α	Mo *K*α
μ (mm^{-1})	0.09	0.09
Crystal shape	Plate	Prism
Color	Colorless	Colorless
Crystal size (mm)	0.12 × 0.08 × 0.01	0.38 × 0.20 × 0.14
Absorption correction	Multi-scan	Multi-scan
T_{min}, T_{max}	0.063, 1.000	0.534, 1.000
No. of measured, independent and observed [$I > 2s(I)$] reflections	9053, 1869, 945	51723, 9867, 7643
R_{int}	0.226	0.084
Θ_{max} (°)	18.9	25.7
Range of *h*, *k*, *l*	*h* = −26→26, *k* = −6→6, *l* = −21→19	*h* = −20→20, *k* = −22→22, *l* = −22→22
$R[F^2 > 2s(F^2)]$, $wR(F^2)$, *S*	0.099, 0.279, 0.98	0.048, 0.135, 1.02
No. of reflections	1869	9867
No. of parameters	253	588
$\Delta\rho_{max}$, $\Delta\rho_{min}$ (e Å^{-3})	0.31, −0.46	0.36, −0.27

Computer programs: *X-AREA* (*Stoe & Cie*, 2001), *CrysAlis PRO* 1.171.42.43a (*Rigaku OD*, 2022), *SHELXS* (G. M. Sheldrick, 1997), *SHELXT* (G. M. Sheldrick, 2015), *SHELXL-2018*/3 (Sheldrick, 2018).

Table S5: Selected crystallographic data for $(\mathbf{3})_2$ and **4**·py.

	$(\mathbf{3})_2$	**4**·py
Chemical formula	$C_{40}H_{48}Al_4Br_8$	$C_{25}H_{29}AlBrN$
M_r	1275.98	450.38
Crystal system, space group	Triclinic, $P\bar{1}$	Triclinic, $P\bar{1}$
Temperature (K)	173	173
a, b, c (Å)	10.6406(6), 11.0267(8), 11.4135(7)	8.8787(6), 9.5697(7), 14.8476(9)
α, β, γ (°)	106.286(6), 94.576(5), 104.445(6)	75.692(6), 75.093(5), 76.432(6)
V (Å^3)	1228.53(15)	1161.41(14)
Z	1	2
F(000)	620	468
D_x (Mg m^{-3})	1.725	1.288
Radiation type	Mo $K\alpha$	Mo Ka
μ (mm^{-1})	6.63	1.82
Crystal shape	Plate	Plate
Color	Colorless	Colorless
Crystal size (mm)	0.28 × 0.16 × 0.06	0.23 × 0.20 × 0.09
Absorption correction	Multi-scan	Multi-scan
T_{min}, T_{max}	0.550, 1.000	0.567, 1.000
No. of measured, independent and observed [I > 2s(I)] reflections	11856, 5615, 4214	9419, 4632, 3950
R_{int}	0.069	0.047
Θ_{max} (°)	27.5	26.4
Range of h, k, l	h = −12→13, k = −14→14, l = −14→14	h = −8→11 k = −11→11, l = −17→18
$R[F^2 > 2s(F^2)]$, $wR(F^2)$, S	0.046, 0.086, 1.02	0.036, 0.089, 1.03
No. of reflections	5615	4632
No. of parameters	271	322
$\Delta\rho_{max}$, $\Delta\rho_{min}$ (e Å^{-3})	0.58, −0.54	0.42, −0.34

Computer programs: *X-AREA* (*Stoe & Cie*, 2001), *CrysAlis PRO* 1.171.42.43a (*Rigaku OD*, 2022), *SHELXS* (G. M. Sheldrick, 1997), *SHELXT* (G. M. Sheldrick, 2015), *SHELXL-2018*/3 (Sheldrick, 2018).

Table S6: Selected crystallographic data for [**5**][$AlBr_4$] and [**5**][Br].

	[**5**][$AlBr_4$]	[**5**][Br]
Chemical formula	$[C_{20}H_{20}AlBr_2N_4][AlBr_4]$	$[C_{20}H_{20}AlBr_2N_4][Br]$
M_r	849.82	583.11
Crystal system, space group	Orthorhombic, $Pna2_1$	Orthorhombic, *Pnna*
Temperature (K)	173	173
a, *b*, *c* (Å)	19.2045(15), 15.4711(11), 9.5030(6)	14.1189(5), 7.9834(3), 22.9967(7)
α, β, γ (°)	90, 90, 90	90, 90, 90
V (Å^3)	2823.5(3)	2592.12(15)
Z	4	4
F(000)	1616	1144
D_x (Mg m^{-3})	1.999	1.494
Radiation type	Mo *K*α	Mo *K*α
μ (mm^{-1})	8.61	4.71
Crystal shape	Block	Needle
Color	Colorless	Colorless
Crystal size (mm)	0.23 × 0.19 × 0.18	0.81 × 0.12 × 0.10
Absorption correction	Multi-scan	Multi-scan
T_{min}, T_{max}	0.175, 1.000	0.152, 1.000
No. of measured, independent and observed [$I > 2s(I)$] reflections	18186, 5553, 4600	35509, 2469, 2074
R_{int}	0.095	0.068
Θ_{max} (°)	26.1	25.7
Range of *h*, *k*, *l*	*h* = −20→23, *k* = −19→18, *l* = −11→11	*h* = −16→17, *k* = −9→9, *l* = −28→28
$R[F^2 > 2s(F^2)]$, $wR(F^2)$, *S*	0.082, 0.202, 1.15	0.029, 0.074, 1.05
No. of reflections	5553	2469
No. of parameters	289	132
$\Delta\rho_{max}$, $\Delta\rho_{min}$ (e Å^{-3})	1.64, −2.22	0.92, −0.40
Absolute structure parameter	0.013(15)	-

Computer programs: *X-AREA* (*Stoe & Cie*, 2001), *CrysAlis PRO* 1.171.42.43a (*Rigaku OD*, 2022), *SHELXS* (G. M. Sheldrick, 1997), *SHELXT* (G. M. Sheldrick, 2015), *SHELXL-2018*/3 (Sheldrick, 2018).

Table S7: Selected crystallographic data for **6** × C_6H_6.

	6 × C_6H_6
Chemical formula	$C_{38}H_{53}Al \times C_6H_6$
M_r	614.89
Crystal system, space group	Triclinic, $P\bar{1}$
Temperature (K)	173
a, *b*, *c* (Å)	9.4620(6), 11.3383(6), 19.6914(7)
α, β, γ (°)	79.522(4), 83.939(4), 67.200(5)
V (Å^3)	1913.57 (18)
Z	2
F(000)	672
D_x (Mg m^{-3})	1.067
Radiation type	Mo *K*a
μ (mm^{-1})	0.08
Crystal shape	Block
Color	Colorless
Crystal size (mm)	0.44 × 0.25 × 0.17
Absorption correction	Multi-scan
T_{min}, T_{max}	0.755, 1.000
No. of measured, independent and observed [$I > 2s(I)$] reflections	18902, 9993, 7477
R_{int}	0.045
Θ_{max} (°)	29.1
Range of *h*, *k*, *l*	*h* = −12→12, *k* = −15→15, *l* = −26→24
$R[F^2 > 2s(F^2)]$, $wR(F^2)$, *S*	0.053, 0.145, 1.03
No. of reflections	9993
No. of parameters	475
$\Delta\rho_{max}$, $\Delta\rho_{min}$ (e Å^{-3})	0.34, −0.27

Computer programs: *X-AREA* (*Stoe & Cie*, 2001), *CrysAlis PRO* 1.171.42.43a (*Rigaku OD*, 2022), *SHELXS* (G. M. Sheldrick, 1997), *SHELXT* (G. M. Sheldrick, 2015), *SHELXL-2018*/3 (Sheldrick, 2018).

3.1 Single-crystal X-ray structure analysis of 1

Compound **1** crystallizes without solvent in the triclinic space group $P\bar{1}$ (No. 2) with one crystallographically unique molecule in the general position (Fig. S35).

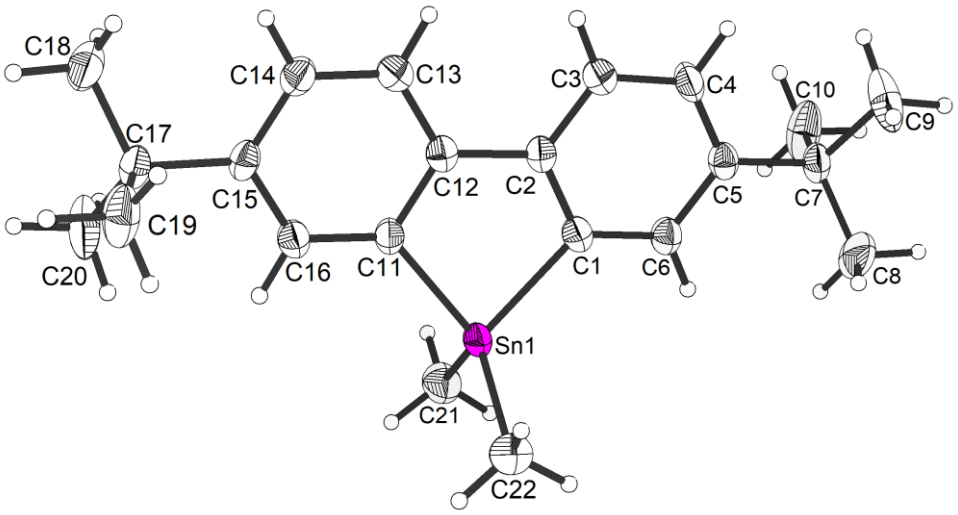

Fig. S35: Molecular structure of **1** in the solid state. Atomic displacement ellipsoids are drawn at the 50 % probability level.

3.2 Single-crystal X-ray structure analyses of two polymorphous modifications of *trans*-(**2**)$_2$

Compound *trans*-(**2**)$_2$ crystallizes without solvent in two polymorphous modifications. The relatively denser α-form crystallizes in the triclinic space group $P\bar{1}$ (No. 2) with one unique molecule in the general position and another at the inversion center, resulting in a rather peculiar value of $Z = 3$ (Fig. S36). One of the terminal *t*Bu-groups in the second molecule is disordered over two positions with the relative weight of 90:10 %. The β-form crystallizes in the monoclinic space group $P2_1/n$ (No. 14) with one crystallographically unique molecule at the inversion center (Fig. S37). Half of the *t*Bu-groups are also disordered over two positions with the relative weight of 90:10 %.

Analysis of the crystal packing of the polymorphous modifications of *trans*-(**2**)$_2$ shows significant differences (Fig. S38). The molecule of α-*trans*-(**2**)$_2$ form a primitive hexagonal packing (Fig. S38a) with pseudo-hexagonal layers in the *ab* plane. The next layers overlay in a "sphere-above-sphere" mode, *i.e.* the layers are not shifted relative to each other. A packing of this type, which is less dense than the expected hexagonal closest one, is rather rare. The distances between the centers of the molecules vary between 6.68 and 11.29 Å in the layer and 14.02 Å between the layers. In contrast, the molecules in the less dense β-*trans*-(**2**)$_2$ form a distorted cubic closest packing (Fig. S38b). The packing is significantly more uniform, with distances between the centers that vary from 9.25 to 12.01 Å.

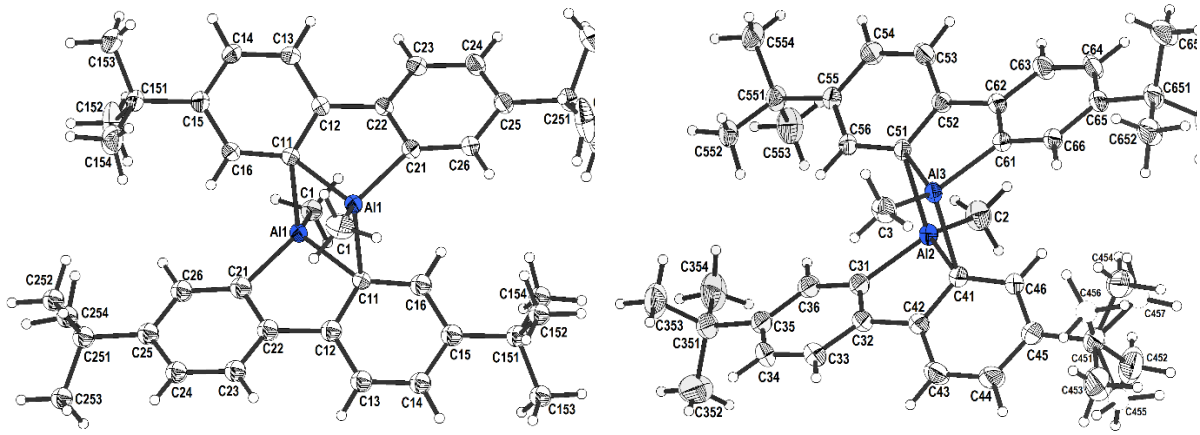

Fig. S36: Molecular structures of two unique molecules in α-*trans*-(**2**)$_2$ in the solid state. Atomic displacement ellipsoids are drawn at the 50 % probability level.

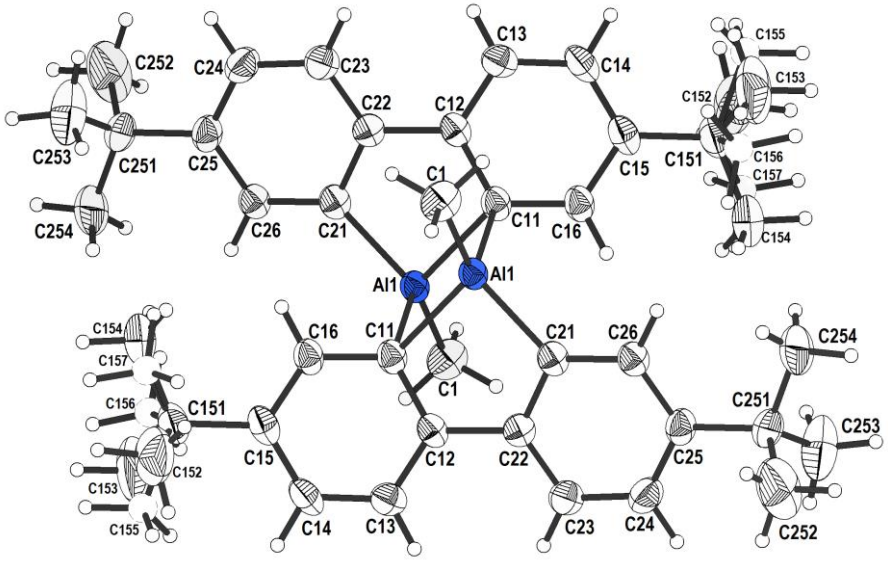

Fig. S37: Molecular structure of β-*trans*-(**2**)$_2$ in the solid state. Atomic displacement ellipsoids are drawn at the 50 % probability level.

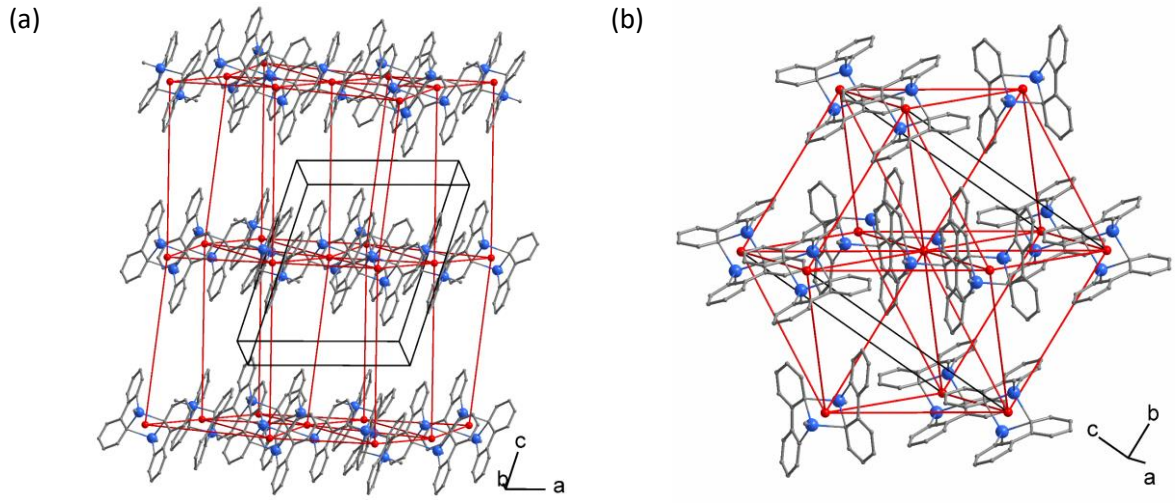

Fig. S38: Packing of (a) α-*trans*-(**2**)$_2$ and (b) β-*trans*-(**2**)$_2$ in the solid state. Terminal *t*Bu-groups as well as H atoms are omitted for clarity. Red lines show the shortest distances between the centers of the molecules.

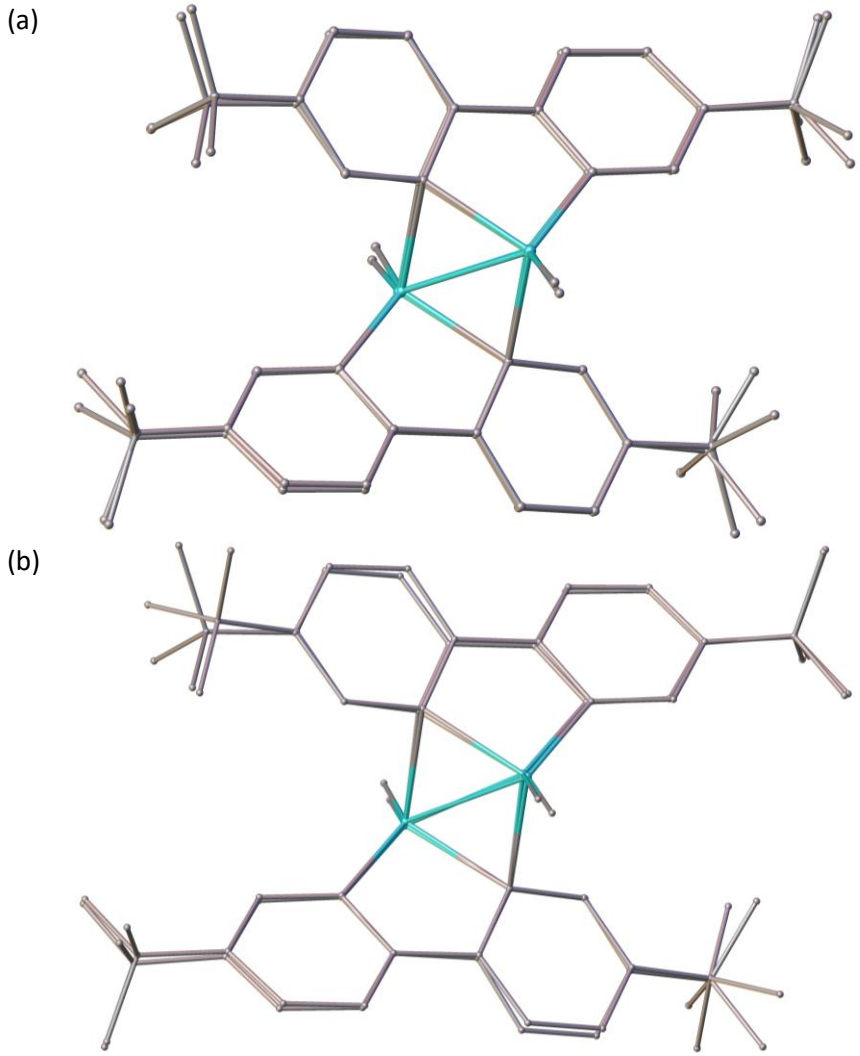

Fig. S39: Overlay of (a) the two crystallographically unique molecules in α-*trans*-(**2**)$_2$ and (b) α-*trans*-(**2**)$_2$ and β-*trans*-(**2**)$_2$ in the unit cell. H atoms omitted for clarity. C: grey, Al: turquoise.

3.3 Single-crystal X-ray structure analysis of 2·OEt_2

Compound **2**·OEt_2 crystallizes without solvent in the monoclinic space group *C*2/*c* (No. 15) with one crystallographically unique molecule in the general position (Fig. S40). Due to the rather poor crystal quality and the weak scattering ability, all reflections above d_{min} = 1.1 Å were omitted from the refinement.

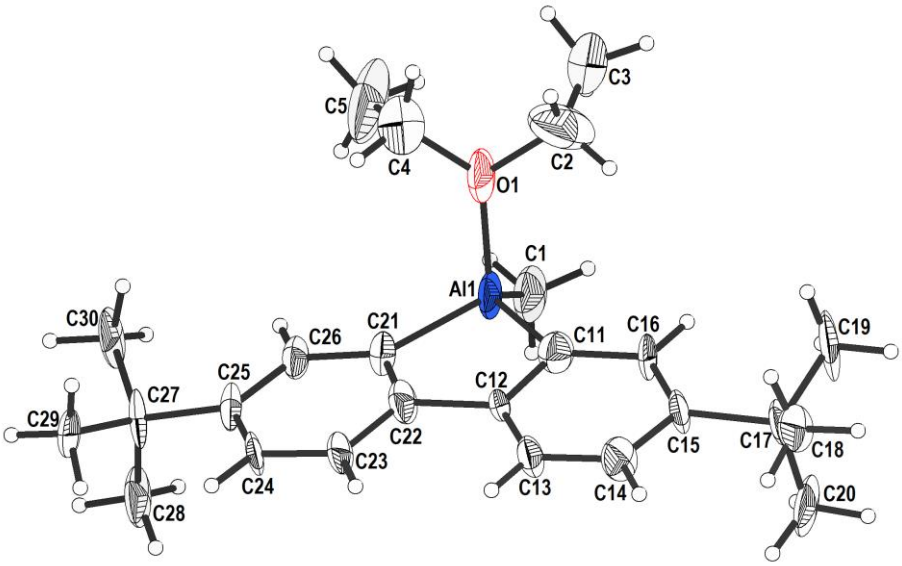

Fig. S40: Molecular structure of **2**·OEt_2 in the solid state. Atomic displacement ellipsoids are drawn at the 50 % probability level.

3.4 Single-crystal X-ray structure analysis of 2·py × $(C_6H_6)_{0.5}$

Compound **2**·py crystallizes as a solvate with one C_6H_6 molecule in the monoclinic space group $P2_1/n$ (No. 14) with two crystallographically unique molecules in the general position (Fig. S41).

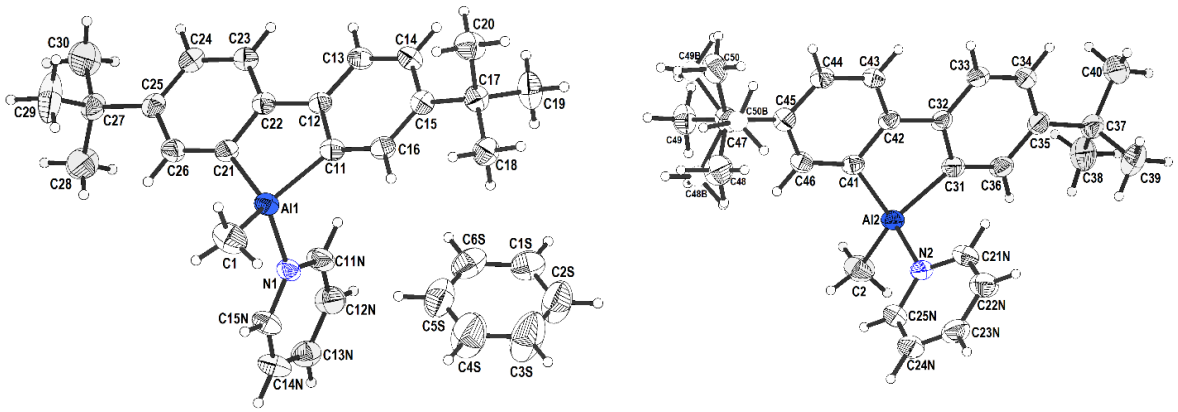

Fig. S41: Molecular structures of two unique molecules of **2**·py × $(C_6H_6)_{0.5}$ in the solid state. Atomic displacement ellipsoids are drawn at the 50 % probability level.

3.5 Single-crystal X-ray structure analysis of $(3)_2$

Compound $(\mathbf{3})_2$ crystallizes without solvent in the triclinic space group $P\bar{1}$ (No. 2) with one crystallographically unique molecule at the inversion center (Fig. S42). Half of the *t*Bu-groups are rotationally disordered over two positions with the relative weight of 70:30 %.

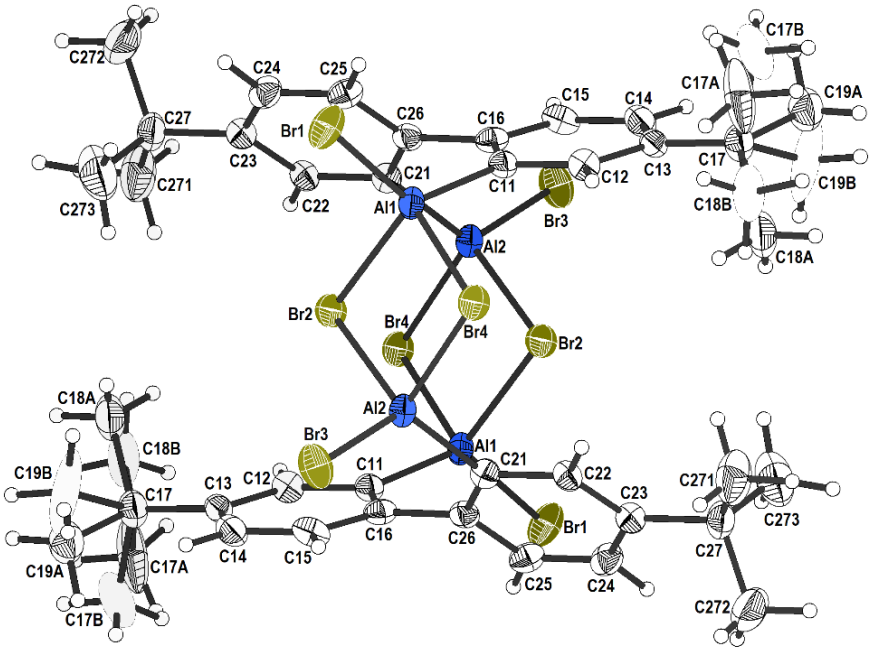

Fig. S42: Molecular structure of $(\mathbf{3})_2$ in the solid state. Atomic displacement ellipsoids are drawn at the 50 % probability level.

3.6 Single-crystal X-ray structure analysis of 4·py

Compound **4**·py crystallizes without solvent in the triclinic space group $P\bar{1}$ (No. 2) with one crystallographically unique molecule in the general position (Fig. S43). One of the *t*Bu-groups is rotationally disordered over three positions with the relative weight of 65.9:20.2:13.9 %.

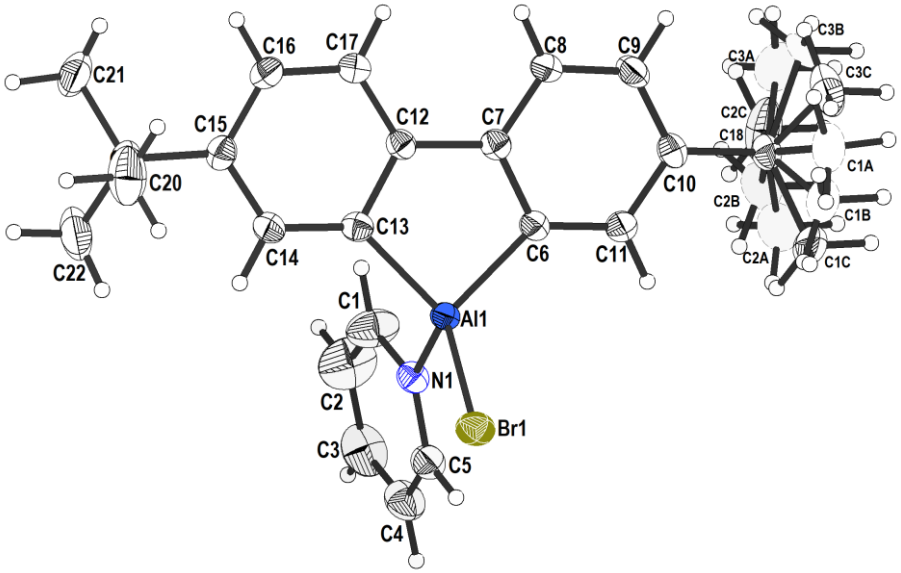

Fig. S43: Molecular structure of **4**·py in the solid state. Atomic displacement ellipsoids are drawn at the 50 % probability level.

3.7 Single-crystal X-ray structure analysis of [5][AlBr$_4$]

Compound [**5**][AlBr$_4$] crystallizes without solvent in the orthorhombic space group *Pna*2$_1$ (No. 33); the cation and anion are both in general positions (Fig. S44).

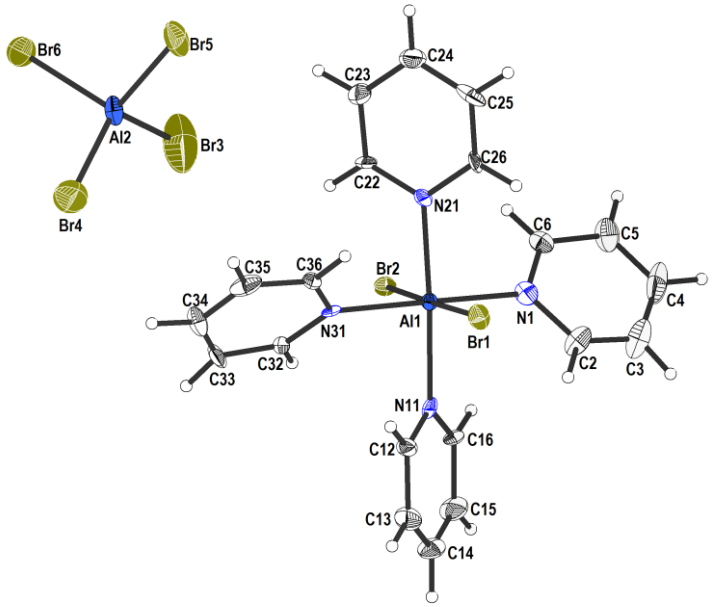

Fig. S44: Molecular structure of [**5**][AlBr$_4$] in the solid state. Atomic displacement ellipsoids are drawn at the 50 % probability level.

3.8 Single-crystal X-ray structure analysis of [5][Br]

Compound [**5**][Br] crystallizes without solvent in the orthorhombic space group *Pnna* (No. 52). The cation is located on the two-fold axis parallel to *c*, while the anion lies on the two-fold axis parallel to *a* (Fig. S45). The residual density map (Δρ map) contains a relatively strong peak Q1, 3.1 e·Å^{-1}, near the terminal Br atom, Br1. It cannot be explained by the disorder of the $AlBr_2$ fragment, since the Al1-Q1 distance is non-bonding (3.19 Å). However, the *x* and *z* coordinates of Q1 almost coincide with those of Br1, while the *y* coordinate can be calculated as ≈1.5−*y*(Br1). Therefore, we can assume that Q1 corresponds to a "shadow" of the entire structure, which is reflected by an additional mirror plane perpendicular to the *b* axis and at *y* = 3/4. This axis contradicts the *Pnna* space group and could indicate the phenomenon of a so-called order-disorder (OD) phenomenon, in which two different polytypes intergrow in the same crystal, leading to stacking faults.[S14] It is remarkable that Al1 and Br2 have y = 0.5 and 0.75 and therefore their "reflection" does not result in any additional peaks. According to this hypothesis, Q1 was assigned to Br1b, and its relative site occupancy factor (sof) was refined to 5 % and then fixed. Due to the very low weight (5 %) of the second polytype, the remaining atoms are not visible on the Δρ map.

During refinement, Br1a was refined anisotropically with sof = 0.95 and Br1b isotropically with sof = 0.05. At this stage, the Platon program revealed two solvent accessible voids of 219 Å^3 containing 51 electrons each. No reliable electron density was found after the OD phenomenon was modelled, and in the final stage of the refinement, Platon/SQUEEZE modeled the unclear, disordered solvent.

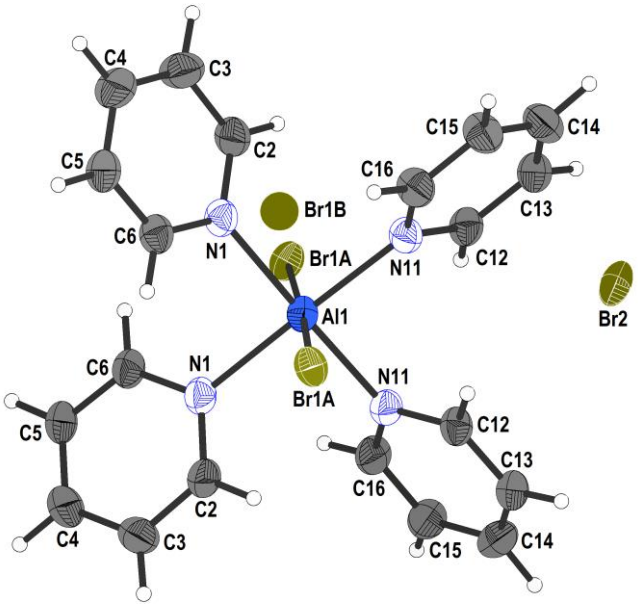

Fig. S45: Molecular structure of [**5**][Br] in the solid state. Atomic displacement ellipsoids are drawn at the 50 % probability level.

3.9 Single-crystal X-ray structure analysis of 6 × C_6H_6

Compound **6** crystallizes as a solvate with one C_6H_6 molecule in the triclinic space group $P\bar{1}$ (No. 2) with one crystallographically unique molecule in the general position (Fig. S46). The C_6H_6 molecule is positionally disordered over two positions with the relative weight of 75:25 %.

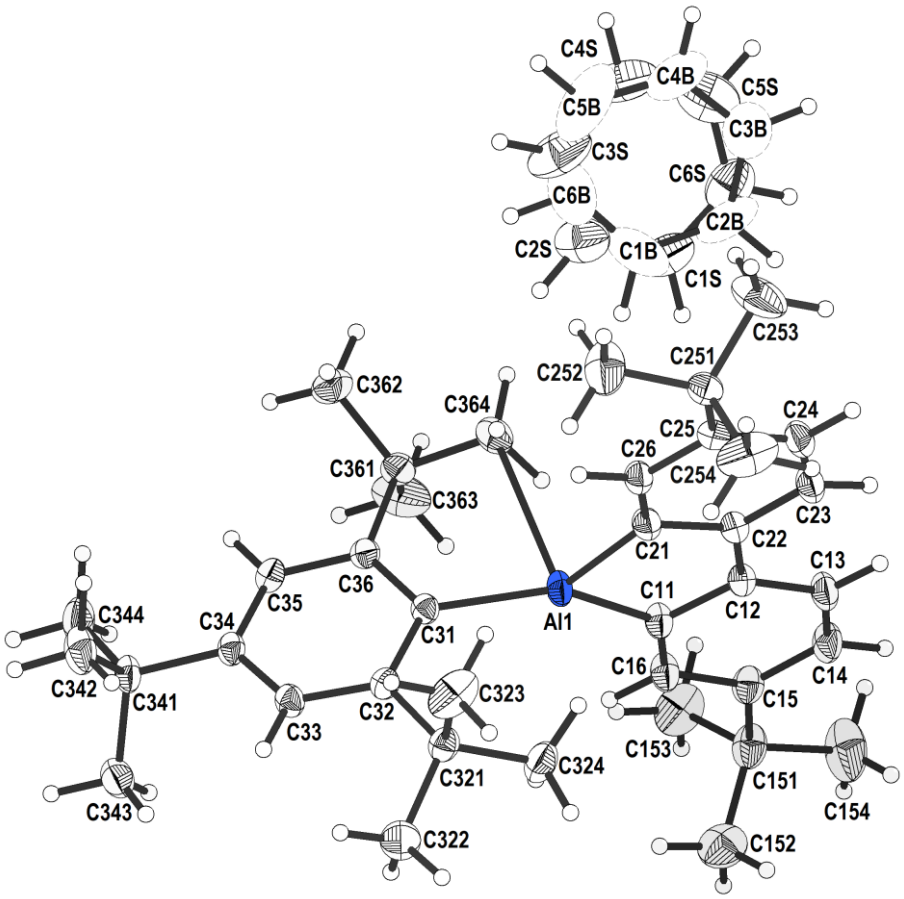

Fig. S46: Molecular structure of **6** × C_6H_6 in the solid state. Atomic displacement ellipsoids are drawn at the 50 % probability level.

4 Computational details

All DFT calculations were performed using *Gaussian 16, Revision B.01*.[S15] Graphical representations of molecular geometries were produced with the *CYLview20* software.[S16]

Geometry optimizations and Hessian calculations were performed at the ωB97XD[S17]/def2-TZVPP[S18] level of theory including implicit solvation by the solvent model based on density (SMD; solvent = CH_2Cl_2).[S19] Optimized geometries were confirmed to be the desired minimum energy structures or transition states by vibrational frequency analysis. Single-point calculations were performed at the SMD(CH_2Cl_2)/ωB97XD/def2-QZVPP[S20] level. A concentration correction accounting for the change in standard states going from gas phase to condensed phase was neglected in the given G_{298} values, since there is no change in moles in the course of the computed rearrangement.

^{13}C NMR isotropic shielding tensors (IST) were computed using the continuous set of gauge transformation (CSGT) method with the SMD(CH_2Cl_2)/LC-TPSSTPSS[S21]/cc-pVTZ[S22,S23] level of theory, as this combination was shown to deliver reliable results in a recent benchmark study.[S24] Since the experimentally observed NMR shift values refer to symmetry-averaged molecular structures, the computed ISTs were averaged over all symmetry-related positions for the nuclei under consideration in each molecule (IST_{av}). ^{13}C NMR resonances were referenced against $SiMe_4$ (IST_{av} = 197.8 ppm; equation (1)), for which optimization and chemical shielding was calculated in the same manner.

$$\delta_{\mathrm{calc}}(^{13}\mathrm{C}) = \mathrm{IST}_{\mathrm{av}}(\mathrm{SiMe_4}) - \mathrm{IST}_{\mathrm{av}}(^{13}\mathrm{C}) \qquad (1)$$

$$\delta_{\mathrm{corr}}(^{13}\mathrm{C}) = 0.9141 \cdot \delta_{\mathrm{calc}}(^{13}\mathrm{C}) - 0.8394 \qquad (2)$$

The calculated NMR shift values $\delta_{calc}(^{13}C)$ were further corrected by applying a compensating linear scaling approach using equation (2). The correction factors were determined using the crystallographically characterized **2**·OEt_2 as a benchmark molecule (Table S8), where only the C atoms of the Me-AlFlu moiety were considered. Fig. S47 shows the calculated uncorrected ^{13}C NMR shift values of the benchmark molecule (x-axis) plotted against the experimentally observed NMR shifts (y-axis).

Table S8: Calculated isotropic shielding tensors (IST_{av}), calculated NMR shift values $\delta_{calc}(^{13}C)$, and experimental NMR shift values $\delta_{exp}(^{13}C)$ (bottom) [ppm] for the relevant ^{13}C nuclei of the benchmark molecule **2**·OEt_2.

C atom	IST_{av} / ppm	$\delta_{calc}(^{13}C)$ / ppm	$\delta_{exp}(^{13}C)$ / ppm
1	53.5	144.3	132.9
2	35.3	162.4	147.9
3	56.8	140.9	125.1
4	64.3	133.4	119.5
5	35.0	162.8	149.0
6	36.5	161.3	147.0
7	159.3	38.5	34.3
8	165.1	32.7	31.2
9	209.2	−11.5	−12.5

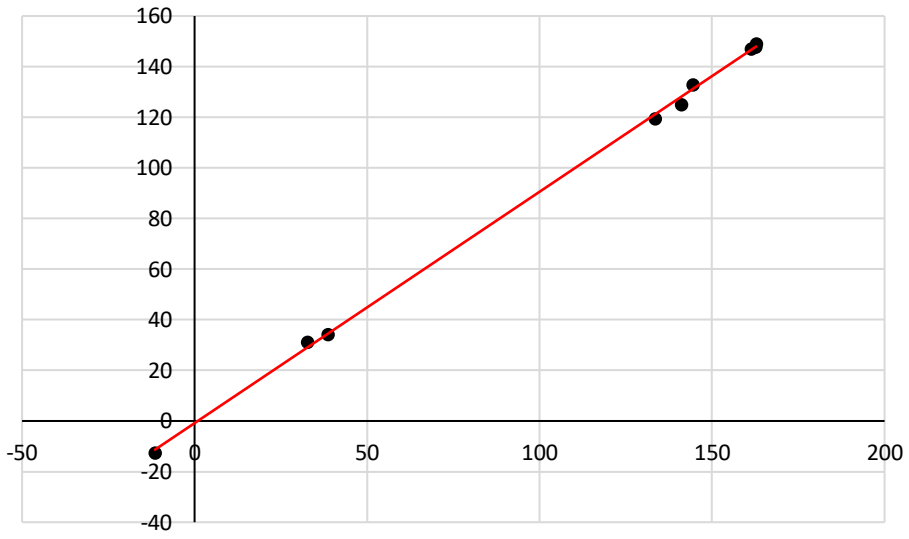

Fig. S47: Plot of the calculated ^{13}C NMR shift values (Table S2; x-axis, ppm) of the benchmark molecule **2**·OEt_2 against the corresponding experimentally determined shift values (Table S2; y-axis, ppm). The linear regression is $f(x) = 0.9141x - 0.8394$ with a certainty of $R^2 = 0.999$.

4.1 Dynamic rearrangement of $(2)_2$

The computed energy difference between the two isomers of $(\mathbf{2})_2$ in CH_2Cl_2 is quite small (ΔG^0 = 1.6 kcal mol^{-1}; Scheme S1). This agrees well with the experimentally determined value at −30 °C (ΔG^0 = 0.7 kcal mol^{-1}; equation (3) and (4)),[S25] which is calculated from the proton-integral ratio K of *cis*-$(\mathbf{2})_2$ and *trans*-$(\mathbf{2})_2$ in CD_2Cl_2. The computed energy of the transition state (TS) for the *cis*/*trans*-equilibrium in CH_2Cl_2 is $\Delta G^{\ddagger}$ = 14.8 kcal mol^{-1}, which again agrees well with the experimentally determined value of $\Delta G^{\ddagger}$ = 14.5 kcal mol^{-1}, derived from the coalescence temperature (T_c):[S27] T_c is used in conjunction with the maximum peak separation in the slow-exchange limit ($\Delta\nu$ = 20.7 Hz is the distance between the *t*Bu resonances of *trans*-$(\mathbf{2})_2$ at −30 °C; Fig. S11, S13). $\Delta G^{\ddagger}$ is then calculated according to equation (5).[S26]

$$\mathrm{K} = \frac{[\textit{cis}\text{-}(\mathbf{2})_2]}{[\textit{trans}\text{-}(\mathbf{2})_2]} \qquad (3)$$

$$\Delta G° = -\mathrm{R}T\ln(\mathrm{K}) \qquad (4)$$

$$\Delta G^{\ddagger} = aT_c[9.972 + \log\left(\frac{T_c}{\Delta\nu}\right)] \qquad (5)$$

where $a = 4.575 \cdot 10^{-3}$ kcal mol^{-1}, T_c = 286 K, $\Delta\nu$ = 20.7 Hz

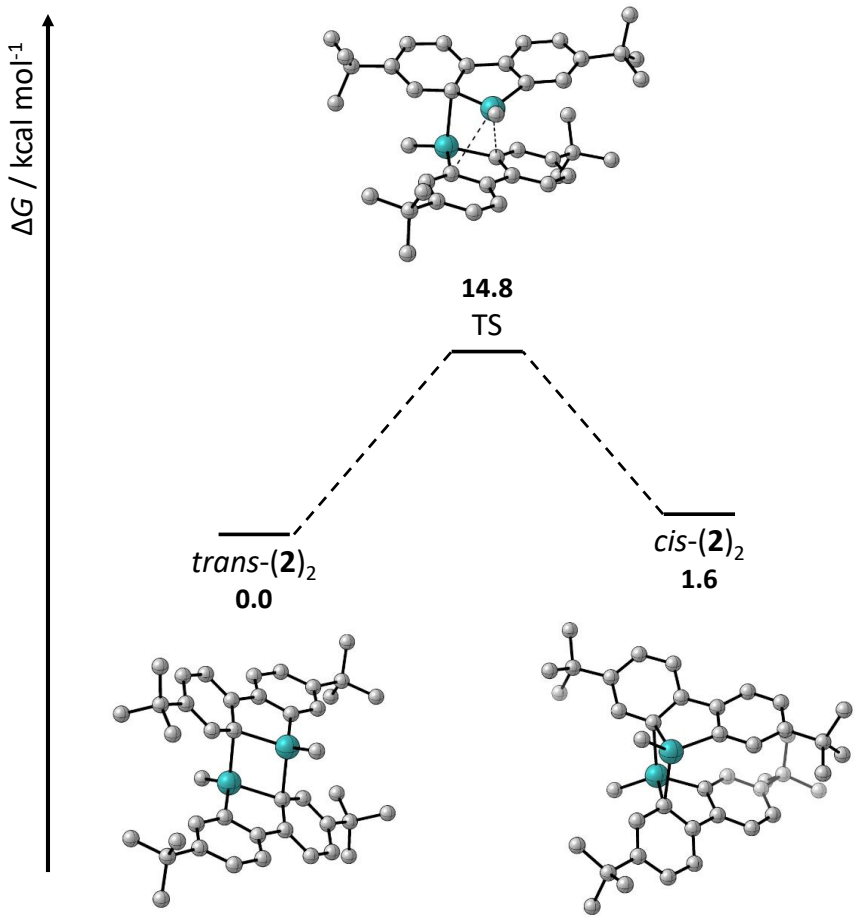

Scheme S1: Computed rearrangement equilibrium between *cis*-$(\mathbf{2})_2$ and *trans*-$(\mathbf{2})_2$ in CH_2Cl_2.

4.2 ^{13}C NMR shift calculations

To further verify that the minor product observed in the reaction of **1** with $AlMe_3$ is indeed *cis*-(**2**)$_2$, the ^{13}C NMR shift values of *cis*-(**2**)$_2$ and *trans*-(**2**)$_2$ (Table S9) were calculated and compared with the experimentally observed shift values of both species.

To obtain as meaningful a picture as possible, only those C atoms were taken into account whose corrected calculated NMR shift values $\delta_{corr}(^{13}C)$ differ by > 1.0 ppm between the two isomers (Table S9; highlighted in yellow). For those, *trans*-(**2**)$_2$ shows a variation from its experimentally observed NMR shift values with an average absolute deviation of 2.1 ppm (Table S10). The variation observed for *cis*-(**2**)$_2$ is even smaller, with an average absolute variation of 1.5 ppm. (Table S11). Reverse assignment (*i.e.*, calculated *cis*-(**2**)$_2$ compared to experimentally observed *trans*-(**2**)$_2$ and vice versa) leads to higher deviations 2.5 and 3.2 ppm (exp. *trans*-(**2**)$_2$ → calc. *cis*-(**2**)$_2$; exp. *cis*-(**2**)$_2$ → calc. *trans*-(**2**)$_2$). In particular, the ^{13}C NMR shift values of the Me-groups at positions 9/9', which differ significantly between the two isomers, are among the best matches of the corrected calculated and experimentally observed shifts. This also supports the above-mentioned assignments of the two isomers.

Table S9: Calculated isotropic shielding tensors (IST_{av}), calculated NMR shift values $\delta_{calc}(^{13}C)$, and corrected calculated NMR shift values $\delta_{corr}(^{13}C)$ [ppm] for all C atoms of *cis*-(**2**)$_2$ and *trans*-(**2**)$_2$. The last column shows the absolute difference between the computed chemical shift values of both isomers; C atoms whose chemical shift values differ by > 1.0 ppm are highlighted in yellow. Solvent model: SMD(CH_2Cl_2).

C atom	*cis*-(**2**)$_2$			*trans*-(**2**)$_2$			Abs. diff. / ppm
	IST_{av} / ppm	$\delta_{calc}(^{13}C)$ / ppm	$\delta_{corr}(^{13}C)$ / ppm	IST_{av} / ppm	$\delta_{calc}(^{13}C)$ / ppm	δ_{corr} (^{13}C) / ppm	
1	51.3	146.5	133.1	50.3	147.4	133.9	0.8
2	34.7	163.0	148.2	33.4	164.4	149.4	1.2
3	57.8	139.9	127.0	55.6	142.1	129.1	2.1
4	61.4	136.4	123.8	61.3	136.5	123.9	0.1
5	37.2	160.5	145.9	36.5	161.3	146.6	0.7
6	33.8	164.0	149.1	30.1	167.7	152.5	3.4
7	159.6	38.1	34.0	158.8	38.9	34.7	0.7
8	165.2	32.5	28.9	165.3	32.4	28.8	0.1
9/9’	205.4	−7.6	−7.8	210.1	−12.4	−12.2	4.4
1’	31.8	165.9	150.8	34.3	163.4	148.5	2.3
2’	36.5	161.3	146.6	35.8	161.9	147.2	0.6
3’	46.5	151.2	137.4	44.8	152.9	138.9	1.5
4’	60.2	137.6	124.9	60.2	137.6	124.9	0
5’	18.8	178.9	162.7	16.6	181.2	164.8	2.1
6’	62.5	135.3	122.8	62.7	135.1	122.7	0.1
7’	159.0	38.7	34.5	158.8	38.9	34.7	0.2
8’	165.3	32.5	28.9	164.7	33.0	29.3	0.4

Table S10: Comparison of the corrected calculated ^{13}C NMR shifts of *cis*-(**2**)$_2$ and *trans*-(**2**)$_2$ with the experimentally observed shifts (CD_2Cl_2) of the main product of the reaction between **1** and $AlMe_3$ (*trans*-(**2**)$_2$). Only the resonances of the C atoms for which the corrected calculated shifts of *cis*-(**2**)$_2$ and *trans*-(**2**)$_2$ differ > 1.0 ppm are considered.

C atom	$\delta_{exp}(^{13}C)$ of *trans*-(**2**)$_2$ / ppm	*cis*-(**2**)$_2$		*trans*-(**2**)$_2$	
		$\delta_{corr}(^{13}C)$ / ppm	Δ ($\delta_{corr} - \delta_{exp}$) / ppm	δ_{corr} (^{13}C) / ppm	Δ ($\delta_{corr} - \delta_{exp}$) / ppm
2	149.2	148.2	1.0	149.4	0.2
3	127.0	127.0	0.0	129.1	2.1
6	151.6	149.1	2.5	152.5	0.9
9/9’	−11.6	−7.8	3.8	−12.2	0.6
1’	145.8	150.8	5.0	148.5	2.7
3’	133.7	137.4	3.7	138.9	5.2
5’	161.5	162.7	1.2	164.8	3.3
Avg. abs. Δ / ppm		**2.5**		**2.1**	

Table S11: Comparison of the corrected calculated ^{13}C NMR shifts of *cis*-(**2**)$_2$ and *trans*-(**2**)$_2$ with the experimentally observed shifts (CD_2Cl_2) of the minor product of the reaction between **1** and $AlMe_3$ (*cis*-(**2**)$_2$). Only the resonances of the C atoms for which the corrected calculated shifts of *cis*-(**2**)$_2$ and *trans*-(**2**)$_2$ differ > 1.0 ppm are considered.

C atom	$\delta_{exp}(^{13}C)$ of *cis*-(**2**)$_2$ / ppm	*cis*-(**2**)$_2$		*trans*-(**2**)$_2$	
		$\delta_{corr}(^{13}C)$ / ppm	Δ ($\delta_{corr} - \delta_{exp}$) / ppm	δ_{corr} (^{13}C) / ppm	Δ ($\delta_{corr} - \delta_{exp}$) / ppm
2	148.0	148.2	0.2	149.4	1.4
3	125.1	127.0	1.9	129.1	4.0
6	148.7	149.1	0.4	152.5	3.8
9/9’	−8.0	−7.8	0.2	−12.2	4.2
1’	147.6	150.8	3.2	148.5	0.9
3’	133.3	137.4	4.1	138.9	5.6
5’	162.1	162.7	0.6	164.8	2.7
Avg. abs. Δ / ppm		**1.5**		**3.2**	

4.3 Computed structures and free energy values

2·OEt_2
G_{298} = –1292.321444 Hartree

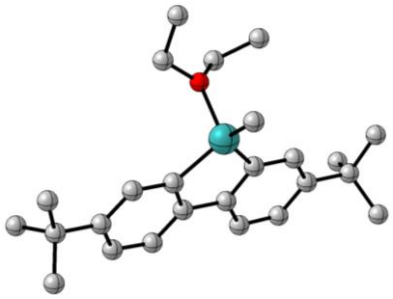

trans-(**2**)$_2$
G_{298} = –2117.449560 Hartree

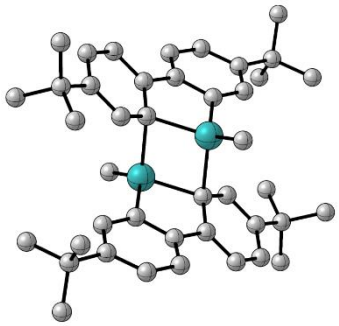

TS
G_{298} = –2117.425978 Hartree

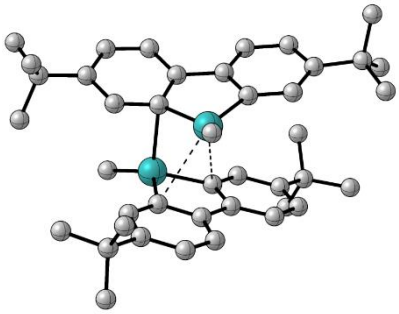

cis-(**2**)$_2$
G_{298} = –2117.446995 Hartree

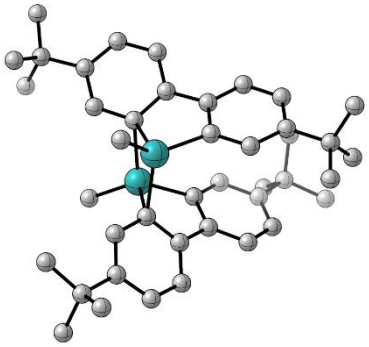

2
G_{298} = –2117.418679 Hartree

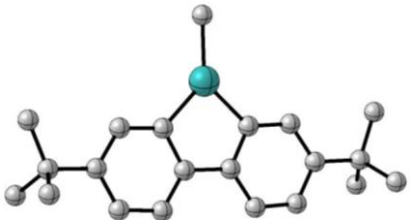

5 References

S1 A. John, S. Kirschner, M. K. Fengel, M. Bolte, H.-W. Lerner and M. Wagner, Simultaneous expansion of 9,10 boron-doped anthracene in longitudinal and lateral directions, *Dalton Trans.*, 2019, **48**, 1871–1877.

S2 A. Hübner, A. M. Diehl, M. Bolte, H.-W.-Lerner and M. Wagner, High-Temperature Reactivity of the Strongly Electrophilic Pristine 9*H*-9-Borafluorene, *Organometallics*, 2013, **32**, 6827–6833.

S3 G. Fraenkel, S. Subramanian and A. Chow, The Carbon–Lithium Bond in Monomeric Aryllithiums: Dynamics of Exchange, Relaxation, and Rotation, *J. Am. Chem. Soc.*, 1995, **117**, 6300–6307.

S4 G. R. Fulmer, A. J. M. Miller, N. H. Sherden, H. E. Gottlieb, A. Nudelman, B. M. Stoltz, J. E. Bercaw and K. I. Goldberg, NMR Chemical Shifts of Trace Impurities: Common Laboratory Solvents, Organics, and Gases in Deuterated Solvents Relevant to the Organometallic Chemist, *Organometallics*, 2010, **29**, 2176–2179.

S5 P. E. Romero, W. E. Piers, S. A. Decker, D. Chau, T. K. Woo and M. Parvez, η^1 versus η^5 Bonding Modes in Cp*Al(I) Adducts of 9-Borafluorenes, *Organometallics*, 2003, **22**, 1266–1274.

S6 B. Kumar, C. E. Strasser and B. T. King, *t*-Butyl Biphenylation of *o*-Dibromoarenes: A Route to Soluble Polycyclic Aromatic Hydrocarbons, *J. Org. Chem.*, 2012, **77**, 311–316.

S7 We are aware that the compounds $AlMe_3$, $AlBr_3$, and $MeAlBr_2$ are not monomeric in solution or in the solid state. However, for simplicity, the monomeric forms were used in calculating the quantities employed.

S8 L. B. Kier, Quantitation of Solvent Polarity Based on Molecular Structure, *J. Pharm. Sci.*, 1981, **70**, 930–933.

S9 M. D. Hanwell, D. E. Curtis, D. C. Lonie, T. Vandermeersch, E. Zurek and G. R. Hutchison, Avogadro: an advanced semantic chemical editor, visualization, and analysis platform, *J. Cheminformatics*, 2012, **4**, 17.

S10 G. M. Sheldrick, Crystal structure refinement with SHELXL, *Acta Crystallogr. Section C*, 2015, **71**, 3–8.

S11 G. M. Sheldrick, SHELXT – Integrated space-group and crystal-structure determination, *Acta Crystallogr. Section A*, 2015, **71**, 3–8.

S12 G. M. Sheldrick, SHELXS-97 and SHELXL-97, Program for Crystal Structure Solution and Refinement, Göttingen, Germany, 1997**.**

S13 V. A. Blatov, A. P. Shevchenko and D. M. Proserpio, Applied Topological Analysis of Crystal Structures with the Program Package ToposPro, *Cryst. Growth Des.*, 2014, **14**, 3576–3586.

S14 T. R. Welberry, Diffuse X-ray Scattering and Models of Disorder, Oxford University Press, Oxford, UK, 2010.

S15 Gaussian 16, Revision B.01, M. J. Frisch, G. W. Trucks, H. B. Schlegel, G. E. Scuseria, M. A. Robb, J. R. Cheeseman, G. Scalmani, V. Barone, B. Mennucci, G. A. Petersson, H. Nakatsuji, M. Caricato, X. Li, H. P. Hratchian, A. F. Izmaylov, J. Bloino, G. Zheng, J. L. Sonnenberg, M. Hada, M. Ehara, K. Toyota, R. Fukuda, J. Hasegawa, M. Ishida, T. Nakajima, Y. Honda, O. Kitao, H. Nakai, T. Vreven, J., A. Montgomery Jr., J. E. Peralta, F. Ogliaro, M. Bearpark, J. J. Heyd, E. Brothers, K. N. Kudin, V. N. Staroverov, R. Kobayashi, J. Normand, K. Raghavachari, A. Rendell, J. C. Burant, S. S. Iyengar, J. Tomasi, M. Cossi, N. Rega, J. M. Millam, M. Klene,

J. E. Knox, J. B. Cross, V. Bakken, C. Adamo, J. Jaramillo, R. Gomperts, R. E. Stratmann, O. Yazyev, A. J. Austin, R. Cammi, C. Pomelli, J. W. Ochterski, R. L. Martin, K. Morokuma, V. G. Zakrzewski, G. A. Voth, P. Salvador, J. J. Dannenberg, S. Dapprich, A. D. Daniels, Ö. Farkas, J. B. Foresman, J. V Ortiz, J. Cioslowski and D. J. Fox, Gaussian, Inc., Wallingford, USA, 2016.

S16 C. Y. Legault, CYLview, 1.0b, 2009.

S17 J.-D. Chai and M. Head-Gordon, Long-range corrected hybrid density functionals with damped atom–atom dispersion corrections, *Phys. Chem. Chem. Phys.*, 2008, **10**, 6615–6620.

S18 F. Weigend and R. Ahlrichs, Balanced basis sets of split valence, triple zeta valence and quadruple zeta valence quality for H to Rn: Design and assessment of accuracy, *Phys. Chem. Chem. Phys.*, 2005, **7**, 3297–3305.

S19 A. V. Marenich, C. J. Cramer and D. G. Truhlar, Universal Solvation Model Based on Solute Electron Density and on a Continuum Model of the Solvent Defined by the Bulk Dielectric Constant and Atomic Surface Tensions, *J. Phys. Chem. B*, 2009, **113**, 6378–6396.

S20 F. Weigend, F. Furche and R. Ahlrichs, Gaussian basis sets of quadruple zeta valence quality for atoms H–Kr, *J. Chem. Phys.*, 2003, **119**, 12753–12762.

S21 J. Tao, J. P. Perdew, V. N. Staroverov and G. E. Scuseria, Climbing the Density Functional Ladder: Nonempirical Meta–Generalized Gradient Approximation Designed for Molecules and Solids, *Phys. Rev. Lett.*, 2003, **91**, 146401.

S22 T. H. Dunning, Gaussian basis sets for use in correlated molecular calculations. I. The atoms boron through neon and hydrogen, *J. Chem. Phys.*, 1989, **90**, 1007–1023.

S23 D. E. Woon and T. H. Dunning, Gaussian basis sets for use in correlated molecular calculations. III. The atoms aluminum through argon, *J. Chem. Phys.*, 1993, **98**, 1358–1371.

S24 M. A. Iron, Evaluation of the Factors Impacting the Accuracy of ^{13}C NMR Chemical Shift Predictions using Density Functional Theory–The Advantage of Long-Range Corrected Functionals, *J. Chem. Theory Comput.*, 2017, **13**, 5798–5819.

S25 G. Wedler, *Lehrbuch der Physikalischen Chemie*, WILEY-VCH, Weinheim, Germany, 1997.

S26 H. Günther, *NMR-Spektroskopie: Eine Einführung in Die Protonenresonanz-Spektroskopie Und Ihre Anwendungen in Der Chemie*, Thieme, Stuttgart, Germany, 1983.

S27 H. Kessler, Detection of Hindered Rotation and Inversion by NMR Spectroscopy, *Angew. Chem. Int. Ed.*, 1970, **82**, 237–253.